공학박사학위논문

A STUDY ON THE THERMO/MECHANICAL BEHAVIOR IN FRICTION STIR WELDING OF STEEL

철강의 마찰교반용접에서의 열적/기계적 거동에 대한 연구

2014년 **8**월

서울대학교 대학원

재료공학부

조 훈 휘

A STUDY ON THE THERMO/MECHANICAL BEHAVIOR IN FRICTION STIR WELDING OF STEEL

철강의 마찰교반용접에서의 열적/기계적 거동에 대한 연구

지도교수 한 홍 남

이 논문을 공학박사학위논문으로 제출함
2014년 7월

서울대학교 대학원
재료공학부
조 훈 휘

조훈휘의 박사학위논문을 인준함
2014년 7월

위 원 장 오 규 환 (인)
부 위 원 장 한 홍 남 (인)
위 원 박 은 수 (인)
위 원 홍 성 태 (인)
위 원 강 석 훈 (인)

ABSTRACT

Friction stir welding (FSW) is a solid state joining process invented by The Welding Institute (TWI, UK) in 1991. The process leads to lower residual stress and distortion in comparison with the fusion-based welding processes, since no melting of the material occurs during the process. Also, the process reduces manufacturing costs on account of the elimination of defects, shielding gas, and costly weld preparation. In addition, the process produces high-quality joints with a finer homogeneous microstructure and superior mechanical properties compared with the fusion-based welding processes.

Initially, the FSW process was used only for non-ferrous alloys with a low melting temperature, such as aluminum alloys. In contrast, application of FSW to ferrous alloys including high strength steel with high melting temperatures has been limited due to high temperatures and severe wear conditions induced by the welding tool during the process. However, continued research into this process has brought some success in the joining of ferrous alloys, and this practical success requires a clearer understanding of the FSW joints of ferrous alloys. In this thesis, the thermo/mechanical behavior in FSW of steel is investigated based on the microstructural and numerical approaches. Also, the simulated results are directly compared with the experimental results for validation of the developed model.

Firstly, the microstructural change in the FSWed region of steel, where phase transformation does not occur, is analyzed. High-quality, defect-free welds are successfully produced in 409 ferritic stainless steel by FSW. A remarkably fine-grained microstructure was observed in the stir zone, and the fraction of low angle grain boundary in the stir zone (SZ) significantly increased as compared to that in the base material. An increase in plunging depth led to an increase of the fraction of low angle grain boundary, a decrease in grain size, and an increase in hardness in the stir zone.

Secondly, a three-dimensional thermo-mechanical simulation of FSW processes is carried out for ferritic stainless steel by utilizing an Eulerian finite volume (FV) method under the steady state condition, and the simulation result is compared directly with both the measured temperature histories during FSW and the microstructural changes after FSW. Based on a visco-plastic self-consistent (VPSC) approach for polycrystal, the texture development in the FSWed material is determined from the velocity gradients along the streamlines in the material flow field. The simulation results show that the heat is generated mainly near the interface between the tool and the workpiece, and that the viscosity changes drastically in the vicinity of the boundary between the SZ and the TMAZ. From the predicted streamlines, it can be indicated that the strong material flow mainly develops on the retreating side of the tool. Also, the simulation results show that the shear deformation texture is significantly developed in the FSWed region. The

measured temperatures and microstructural characteristics agree fairly well with the predicted data.

Thirdly, microstructural evolution during FSW of a high-strength linepipe steel with phase transformation is studied. The various grain structures developed through a complex process including the rearrangement of low-angle boundaries, continuous dynamic recrystallization and phase transformation. In most parts of the SZ, acicular-shaped bainitic ferrites were formed by the phase transformation during the FSW process. A fine-grained microstructure developed mainly in the TMAZ, where continuous dynamic recrystallization occurs. The shear texture in the SZ became considerably weak due to the phase transformation during the FSW process. The hardness of the SZ was significantly higher than that of the other FSWed regions due to the bainitic ferrites.

Lastly, the developed thermo-mechanical model is coupled with the phase transformation model. Frictional heat and severe plastic deformation would affect phase transformation behavior of steel during FSW. Thus, the appropriate model is developed using the austenite grain size evolution model. The measured temperatures and phase fraction agree fairly well with the predicted data.

From this study, thermo/mechanical behavior in FSW of steel, which has not been clear up to now, is described well. The developed model and suggested method lead to a clearer understanding about FSW of ferrous alloys.

Furthermore, the rigorous numerical model coupled with experimental results demonstrates sufficient possibilities, which can predict directly the changes of microstructural characteristics during the FSW process.

Keywords: Friction stir welding (FSW), Stir zone (SZ), Thermo-mechanically affected zone (TMAZ), Heat affected zone (HAZ), Ferritic stainless steel, High-strength steel, Continuous dynamic recrystallization, Dynamic recovery, Plunging depth, Thermo-mechanical modeling, Eulerian finite volume (FV) method, Visco-plastic self-consistent (VPSC) approach, Shear texture, Material flow, Viscosity, Plastic deformation, Phase transformation, Acicular-shaped bainitic ferrite, Hardness, Austenite grain size evolution

Student number: 2008-20689

Contents

Chapter 4

Microstructural analysis of friction stir welded steel with phase transformation

LIST OF TABLES

LIST OF FIGURES

SZ. Misorientation-axis distributions are shown in the top right corners of the graphs, respectively.

Figure 4.8 Profiles of grain size and acicular-shaped phase fraction with aspect ratio over 3 measured from the region indicated by the red rectangle in Figure 4.2.

Figure 4.9 Temperature-time profile measured at the root of the tool shoulder.

Figure 4.10 TEM micrographs showing the morphological characteristics of (a) SZ and (b) BM.

Figure 4.11 Characteristic microstructural features of the RS of the SZ: (a) band contrast (BC) map; (b) misorientation-angle distribution (random distribution is shown by a dotted line); (c) {110} pole figure.

Figure 4.12 Cross-sectional macrograph of the welded sample with indentation marks.

(b) FSWed region, respectively. WD, TD and ND correspond to welding, transversal and normal directions, respectively.

Figure 5.8 Computed heat of transformation profile in x = 2.85 mm (yz-plane, xy-plane).

Chapter 1

Introduction

1.1 Friction stir welding (FSW)

Friction stir welding (FSW) is a solid state joining process invented by The Welding Institute (TWI, UK) in 1991. The process leads to lower residual stress and distortion in comparison with the fusion-based welding processes, since no melting of the material occurs during the process. Also, the process reduces manufacturing costs on account of the elimination of defects, shielding gas, and costly weld preparation. In addition, the process produces high-quality joints with a finer homogeneous microstructure and superior mechanical properties compared with the fusion-based welding processes [1,2].

FSW is performed using a rotating and traversing tool consisting of a shoulder with larger diameter and an integral protruding smaller pin (threaded in general). The tool with high rotating speed is plunged with a proper tilt into the joint line and is then traversed along the joint line between the abutting workpieces. Heat is generated by both the friction between the tool and the workpiece and the severe plastic deformation of the material in the vicinity of the joint line. The workpieces are ultimately joined by the stirring action of

the softened material during the process. A schematic illustration of FSW is shown in Figure 1.1.

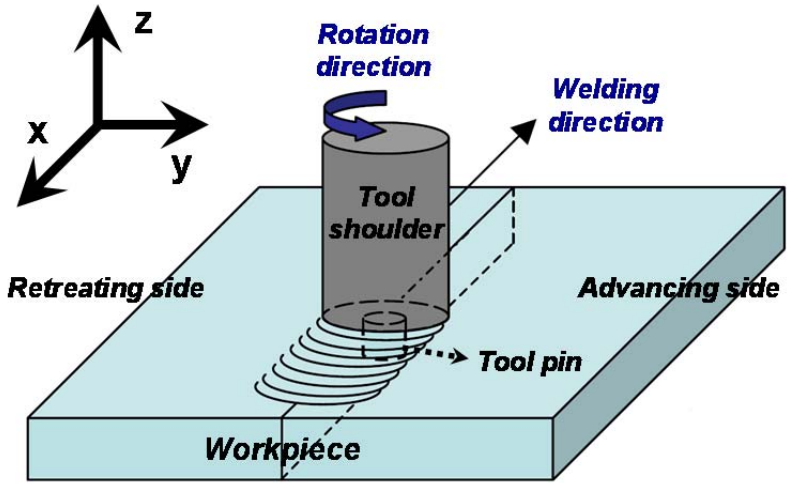

Figure 1.1 A schematic illustration of FSW.

1.2 Application of FSW into steel

In recent years, there has been increasing demand for high-performance steels with high strength, excellent low-temperature toughness, good weldability and superior corrosion resistance because high-performance steels are normally installed in severe environments such as permafrost or seismic regions. Thus, recently, high-performance steel with those properties has been noted in the field of steel manufacturing.

The electric resistance welding (ERW) process is normally used to join normal steel in the manufacturing process due to efficiency and little pollution. However, the heat generated during the ERW process of the steel leads to grain coarsening in the welded region because it solidifies directly from the liquid to ferrite phase without any intermediate phase transformation [3]. Although this steel has useful properties in the wrought condition, the conventional ERW process reduces the toughness, ductility and corrosion resistance of this steel because of grain coarsening during the welding process. Thus, this steel should be joined with a low heat input and high welding speed, and friction stir welding (FSW) has attracted attention as an alternative welding process in the manufacture of a pipeline. Nevertheless, FSW of ferrous alloys has been known to be very difficult for various reasons [4] including high temperatures and severe wear conditions encountered by the welding tool during the process. However, once a cost-effective, adequate

wear resistant tool material becomes available, the desirable qualities of FSW joints [5] and those of ferrous alloys can result in a rapid implementation of FSW of ferrous alloys in various engineering applications including the automotive industry. Continued research into this process has brought some success in the joining of ferrous alloys [6-8], and this practical success requires a clearer understanding of the FSW joints of ferrous alloys.

1.3 Thesis motivations: Clear understanding about FSW

The heat transfer and material flow, which are the key parameters of FSW, vary according to the properties of welded material, the rotation and welding speeds of the tool, and the tool geometry. The complicated interactions among the various physical variables, which occur simultaneously, affect the heating/cooling rates, the material flow during FSW, and the microstructure and properties of the welded joints after FSW.

Since its invention, the FSW method has been widely investigated based on the both microstructural and numerical approaches. Therefore, a fundamental knowledge for the complex physics during FSW should be required, and the rigorous numerical model based on the microstructural results is very suitable in this research.

Firstly, it is very important to understand the microstructural evolution of ferrous alloys during FSW because this understanding would enable a prediction of the weld properties resulting from the microstructures [9,10]. On the other hand, a solid-state phase transformation should be considered in the microstructural evolution of ferrous alloys including mild and high-strenght steel during FSW. This phenomenon is considered as a main factor affecting the properties of ferrous alloys, and studies concerning this phenomenon have been performed by many researchers [11-16].

Secondly, it is also very important to develop numerical models coupled

with experimental data have been reported [17-21]. While several researchers have recently worked on the development of rigorous numerical models considering convective heat transfer due to material flow during FSW[22-36], these numerical studies have not focused on the changes of the microstructural characteristics such as the texture and the geometry of the FSWed region during/after the FSW process.

In this study, microstructural evolution of the FSWed steel is analyzed and a rigorous numerical model coupled and verified with experimental data is developed. These approaches explain well the thermo/mechanical behavior in FSW of steel which has not been clear up to now. In other words, the developed model and suggested method lead to a clearer understanding about FSW of ferrous alloys. Furthermore, this study shows sufficient possibilities, which can predict directly the changes of microstructural characteristics during the FSW process only by using the rigorous numerical model.

1.4 References

[1] Sato YS, Urata M, Kokawa H, Ikeda K, Enomoto M. Scripta Mater 2001;45:109.

[2] Sato YS, Kurihara Y, Park SHC, Kokawa H, Tsuji N. Scripta Mater 2004;50:57.

[3] Folkhard E. Welding Metallurgy of Stainless Steels. first ed. New York: Spring-Verlag Wien; 1988.

[4] Reynolds AP, Tang W, Gnaupel-Herold T, Prask H. Scripta Mater 2003;48:1289.

[5] Sato YS, Nelson TW, Sterling CJ. Acta Mater 2005;53:637.

[6] Sato YS, Yamanoi H, Kokawa H, Furuhara T. Scripta Mater 2007;57:557.

[7] Bhadeshia HKDH, Debroy T. Sci Technol Weld Joi 2009;14:193.

[8] Cho HH, Han HN, Hong ST, Park JH, Kwon YJ, Kim SH, Steel RJ. ater Sci Eng A 2011;528:2889.

[9] Sato YS, Nelson TW, Sterling CJ. Acta Mater 2005;53:637.

[10] Mironov S, Sato YS, Kokawa H. Acta Mater 2008;56:2602.

[11] Han HN, Lee JK. ISIJ Int 2002;42:200.

[12] Han HN, Lee CG, Oh CS, Lee TH, Kim SJ. Acta Mater 2004;52:5203.

[13] Han HN, Lee JK, Suh DW, Kim SJ. Philos Mag 2007;87:159.

[14] Han HN, Lee CG, Suh DW, Kim S-J. Mater Sci Eng A 2008;485:224.

[15] Han HN, Oh CS, Kim G, Kwon O. Mater Sci Eng A 2009;499:462.

[16] Lee MG, Kim SJ, Han HN. Int J Plasticity 2010;26:688.

[17] Frigaard O, Grong O, Midling OT. Metall Mater Trans A 2001;32:1189.

[18] Chao YJ, Qi X, Tang W. J Manuf Sci E-T Asme 2003;125:138.

[19] Song M, Kovacevic R. Int J Mach Tool Manu 2003;43:605.

[20] Song M, Kovacevic R. P I Mech Eng B-J Eng 2004;218:17.

[21] Khandkar MZH, Khan JA, Reynolds AP. Sci Technol Weld Joi 2003;8:165.

[22] Cho JH, Boyce DE, Dawson PR. Mat Sci Eng a-Struct 2005;398:146.

[23] Cho JH, Dawson PR. Metall Mater Trans A 2006;37A:1147.

[24] Hart EW. J Eng Mater-T Asme 1976;98:193.

[25] Seidel TU, Reynolds AP. Sci Technol Weld Joi 2003;8:175.

[26] Ulysse P. Int J Mach Tool Manu 2002;42:1549.

[27] Colegrove PA, Shercliff HR. Sci Technol Weld Joi 2004;9:345.

[28] Colegrove PA, Shercliff HR. Sci Technol Weld Joi 2004;9:352.

[29] Colegrove PA, Shercliff HR. J Mater Process Tech 2005;169:320.

[30] Nandan R, Roy GG, Debroy T. Metall Mater Trans A 2006;37A:1247.

[31] Nandan R, Roy GG, Lienert TJ, DebRoy T. Sci Technol Weld Joi 2006;11:526.

[32] Nandan R, Roy GG, Lienert TJ, Debroy T. Acta Mater 2007;55:883.

[33] Guerdoux S, Fourment L. Model Simul Mater Sc 2009;17.

[34] Assidi M, Fourment L, Guerdoux S, Nelson T. Int J Mach Tool Manu 2010;50:143.

[35] Arora A, Zhang Z, De A, DebRoy T. Scripta Mater 2009;61:863.

[36] Arora A, DebRoy T, Bhadeshia HKDH. Acta Mater 2011;59:2020.

Chapter 2

Microstructural analysis of friction stir welded steel without phase transformation

2.1 Introduction: Microstructural approach

While the development of adequate tool materials for FSW of ferrous alloys is still in progress as mentioned in previous section, pursuing a clear understanding of the characteristic of FSW joints of ferrous alloys is also important. The structure and properties of FSW joints of ferrous alloys, including austenitic SS [1-5] and carbon steels [6,7] have been investigated by various researchers. According to Reynolds et al. [3], a lower energy input due to the lower tool rotation rate during FSW of 304L SS resulted in a lower weld temperature and a finer weld nugget grain size. Sato et al. [4] investigated recrystallization phenomenon during friction stirring of 304L SS by experimental approaches and found that the friction stir processed 304L SS underwent partial static recrystallization following dynamic recrystallization. Sato et al. [5] also investigated microstructure and mechanical properties of FSWed SAF 2507 super duplex SS. They found that FSW refined grains of the ferrite and austenite phases in the stir zone through dynamic recrystallization. As a result of the smaller grain sizes of the ferrite and

austenite phases, the hardness and strength within the stir zone increased.

Fujii et al. [6] investigated the effect of the carbon content and phase transformation on the mechanical properties and microstructures of FSWed carbon steels with various carbon contents. They suggested that when FSW is performed in the two phase region (ferrite + austenite), the microstructure is refined and the highest strength is then achieved. Sato et al. [7] investigated microstructural evolution of ultrahigh carbon steel during FSW. They showed that FSW changed the (ferrite + cementite) duplex structure into a martensitic structure in the weld center. The heat affected zone (HAZ) had a mixed microstructure consisting of both the (ferrite + cementite) duplex structure and the martensitic one. The microstructural evolution of each region was probably due to the solid-state phase transformation during the FSW cooling cycle.

In contrast, application of FSW for ferritic SS is still limited while there is increasing demand of implementation of FSW in the manufacture of automotive parts using ferritic SS especially due to avoiding of solidification problems associated with resistance welding. Furthermore, there have been few papers dealing with FSW of ferritic SS. The studies have examined only the feasibility of FSW in ferritic SS [8,9].

In this study, 409 ferritic SS alloy sheets were subjected to FSW. The microstructural change in the FSWed region depending on two different plunging depths was examined. Reported here are the results of the

investigation of the microstructure of FSW joints of 409 ferritic SS for two different plunging depths.

2.2 Experimental procedure

In this study, 2 mm thick 409 SS plates (nominal chemical composition is listed in Table 2.1) were friction stir butt welded using a convex scrolled shoulder tool made of polycrystalline cubic boron nitride (PCBN). The PCBN tool used in this study had a shoulder diameter of 36.8 mm (at the root of the convex shoulder), a pin diameter of 5.7 mm and a pin length of 1.2 mm. FSW was conducted with the process parameters listed in Table 2.2, i.e., with two different plunging depths, 1.57 and 1.65 mm. Since the PCBN tool used in this research has a convex shoulder, slightly different plunging depths during FSW resulted in somewhat different contact areas between the tool shoulder and the welded material. As a result, different amounts of both heat input and plastic deformation of the material were induced. Throughout the FSW processes, an argon atmosphere was maintained using a gas cup located around the tool to minimize surface oxidation. Also, the temperature during FSW was measured using a thermocouple inserted to the root of the tool shoulder through the tool holder.

Prior to the microstructural analysis, simple quasi-static tensile tests were conducted according to ASTM-E8 using the specimens prepared perpendicular to the FSW direction to confirm a successful joining of the given material. For microstructural analysis of the FSW joints, an EBSD equipped with FE-SEM (SEM: JSM6500F and EBSD: Oxford Inca System)

was used. The specimens were prepared perpendicular to the welding direction. The samples were mechanically ground and electrolytically polished in a 90 ml ethanol + 10 ml perchloric acid solution at 20 V for 30 sec. A Vickers hardness test was performed at the mid-thickness of the weld using a load of 4.9 N and a dwell time of 15 seconds.

Table 2.1 Chemical composition and mechanical properties of 409 stainless steel; Note that the mechanical properties were measured by quasi-static tensile and Vickers hardness tests.

Chemical compositions (wt. %)								
C	Cr	Fe	Mn	Ni	P	S	Si	Ti
≤ 0.08	11.13	86	≤ 1.0	≤ 0.5	≤ 0.045	0.030	≤ 1.0	0.75

Mechanical properties			
Tensile strength* (MPa)	Yield strength* (MPa)	Elongation at fracture* (%)	Vickers hardness (HV)
448	238	32.5	470

*: average of the results of three quasi-static tensile tests.

Table 2.2 Friction stir welding parameters used in the experiments

Specimens	Engage			Traverse	
	Rotation (rpm)	Feed rate (mm/min)	Depth (mm)	Rotation (rpm)	Feed rate (mm/min)
Condition-1	1100	7.62	1.65	600	254
Condition-2	1100	7.62	1.57	600	254

2.3 Microstructural analysis: Steel without phase transformation

FSW successfully produced a defect-free weld in the 409 ferritic SS, as shown in the cross-sectional macrograph in Figure 2.1a. The result of the quasi-static tensile test confirms that the FSW was successful as the failure occurred in the base material for all the specimens tested as shown in Figure 2.1b. The region was confirmed by comparing the tensile strength and hardness shown in later section. In the cross section, the left- and right-hand sides of the weld center correspond to retreating and advancing sides of the rotation tool, respectively. The FSW joint consists of the stir zone (SZ), the base material (BM), the narrow transition region – commonly called thermomechanically affected zone (TMAZ), and the heat affected zone (HAZ) between the TMAZ and BM, even though it is not easy to clearly distinguish each zone. The SZ shows a basin-like shape which widens considerably towards the upper surface. The border region between the SZ and the BM is TMAZ and HAZ, where a transition to the coarse-grained BM microstructure occurs.

Figures 2.2a and b show (i) orientation maps, (ii) misorientation-angle distributions, and (iii) {110} pole figures of the BM (marked as a region 1 in Figure 2.1) and the center region of the SZ (marked as a region 2 in Figure 2.1), respectively. As shown, considerably fine homogeneous grains

developed in the SZ similar to those observed in other steel alloys [3-7]. The fine-grained microstructure in the SZ is due to the dynamic recrystallization induced by severe shear deformation and the significant amount of heat generated during FSW. In the SZ (region 2 in Figure 2.1), the average grain size is about 1.75 μm, which is approximately seven times smaller than that of the BM (region 1 in Figure 2.1). The grain size was measured by linear interception.

The degree of grain refinement observed in the ferritic SS is remarkably higher than that observed in the austenitic SS under similar joining conditions [3-5]. This may be explained by the fact that the stacking fault energy (SFE) of ferritic SS is larger than that of austenitic SS [10,11]. In low SFE materials, dislocation cross-slip is difficult to occur since the partial dislocations are widely separated while their recombination onto the new slip plane requires a considerable amount of energy. With increasing SFE, the partial dislocations become closer together and may recombine readily to facilitate cross-slip. As such, dislocation cell formation is enhanced [10,12]. Thus, in ferritic stainless steel with a relatively large SFE, dislocation cells are more evenly distributed on the whole weld and act as nucleation sites during FSW process. As a result, the larger SFE of the ferritic SS may strongly affect the continuous dynamic recrystallization, resulting in a very fine microstructure.

In the orientation maps in Figures 2.2a and b, the low-angle boundaries (2^o<LABs<15^o) and the high-angle boundaries (HABs>15^o) are depicted as

white and black lines, respectively. The grain boundaries of the BM are composed of mostly HABs and only a few LABs. Misorientation-angle distribution in the BM is very close to a random distribution, which is shown as the dotted line in Figure 2.2a-(ii). In contrast, the fraction of LABs in the SZ is about 54.4%, which is significantly larger than 11.3% in the BM. This indicates that not only dynamic recrystallization but also recovery occurred in the SZ during the FSW process due to the significantly increased temperature of the material [13,14].

Also, in contrast to the largely random texture of the BM, as shown in Figure 2.2a-(iii), the texture of the SZ is consistent with a strong simple shear texture (Figure 2.2b-(iii)). In order to precisely describe a shear texture, it is necessary to define the crystallographic plane {hkl} and direction <uvw> aligned with the shear plane normal (SPN) and shear direction (SD), respectively. According to Mironov et al. [15], the shear plane is presumably parallel to the border between the TMAZ and SZ; thus, the SD is identical to welding direction (WD) on both the retreating and advancing sides, whereas in the central part of the SZ, the SD is parallel to transversal direction (TD). This concept may be applicable to the pole figures in Figure 2.2b. The texture caused by the FSW process is then very similar to a shear texture associated with simple shear deformation of bcc materials [16,17].

It is well known that the applied specific weld energy for FSW is obtained from the quotient of the rotation speed and the welding speed, and

the difference in the energy input is manifested in the resulting temperatures observed during welding [3]. However, the temperature profile of the tool shown in Figure 2.3a suggests that an increase in plunging depth can cause a temperature increase even under the same rotation and welding speeds. Since the PCBN tool has a convex shoulder, the increase in plunging depth increases the contact area between the concave tool shoulder and the material and consequently, increases the heat input to the material during FSW.

According to thermodynamic calculation using Thermo-Calc software, austenite transition temperature of ferritic SS is about 1100 K. During the experiment, the peak temperature measured at the root of the tool shoulder was approximately 930K (Figure 2.3a), which is significantly lower the austenite transition temperature. Even though the temperature of the material during FSW may be slightly higher than that of the root of the tool shoulder, it is unlikely that the temperature of the material during FSW becomes higher than the austenite transition temperature. Even if the temperature of the material reached to the austenite transition temperature during FSW, the cooling was not fast enough to develop austenite-to-martensite transformation. As a result, no martensite transformation was observed in the joint.

Figure 2.3b shows the profiles of the LAB fraction for the two welded specimens with different plunging depths as a function of the distance from the weld centerline. A larger fraction of the LAB was observed in the SZ as compared with the BM in both specimens. Note that the deeper plunging

depth during FSW showed a larger LAB fraction. The LAB fraction would be determined by the amount of recovery in the materials behind the tool pin. Also, the amount of recovery should be affected by the temperature during FSW. Therefore, the increased LAB fraction with deeper plunging depth may be explained by the larger amount of recovery in the SZ induced by a higher temperature during the FSW with the deeper plunging depth.

Figure 2.4 shows profiles of grain size and hardness for the two welded samples with two different plunging depths of 1.57 and 1.65 mm as a function of the distance from the weld centerline. The refinement of the grain size due to FSW increased the hardness of the SZ compared to BM. Though the distribution of grain size is mostly uniform in the SZ, the grain size in the advancing side (AS) is slightly larger than that in the retreating side (RS) as shown in Figure 2.5. It is known that the recrystallized grains are formed in the SZ of a FSW joint, and then undergo grain growth during the cooling cycle [18]. Since grain growth occurs more rapidly at a higher temperature, it may be suspected that the temperature was slightly higher on the advancing side than the retreating side during FSW. This agrees well with the previously reported calculation result [17]. These results also demonstrate that effective carbon diffusion does not occur during FSW since there is no change of hardness induced by carbon concentration gradient. Generally, the effective carbon diffusion would be impeded by severe plastic flow during FSW even if enough time and significant heat is given in the process. Figure 2.4 also shows

that the increase in plunging depth decreased the grain size and increased the hardness in the SZ. This may be explained by the fact that the region of plastic deformation under the tool shoulder became deeper as the plunging depth increased.

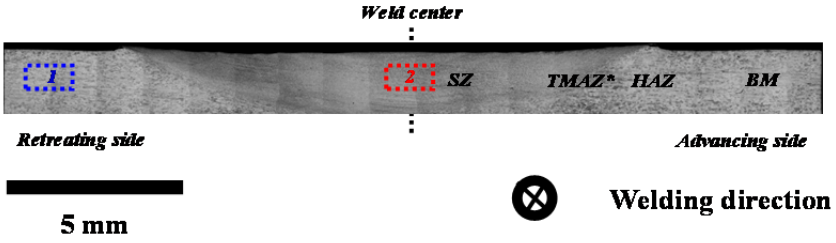

(a)

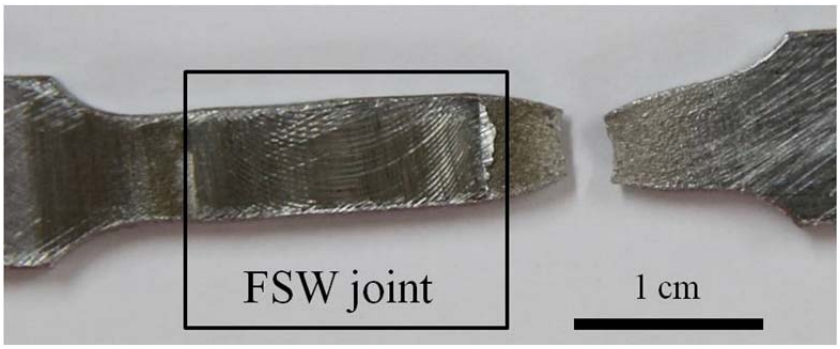

(b)

Figure 2.1 (a) Cross-sectional macrograph of the welded sample (*mark means approximate region) and (b) the FSW specimen with a plunging depth of 1.57 mm after the quasi-static tensile test.

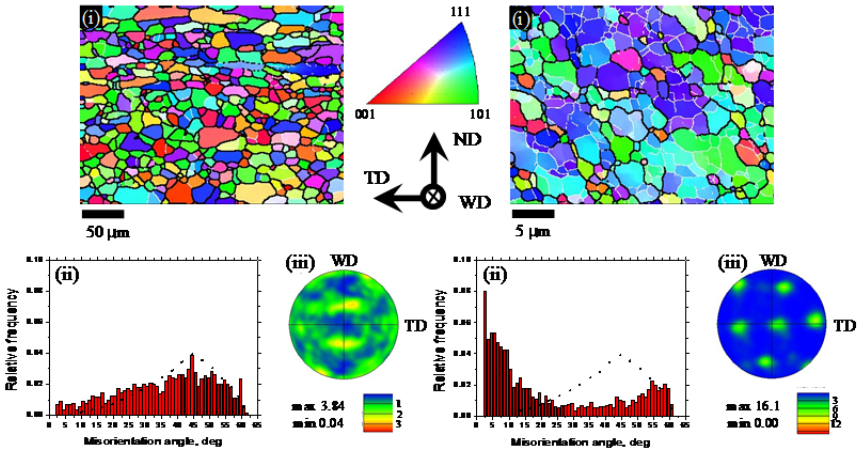

(a) (b)

Figure 2.2 (i) Orientation map, (ii) misorientation-angle distribution (random distribution is shown by a dotted line) and (iii) {110} pole figure of (a) base material (Region 1 in Figure 2.1) and (b) FSWed region (Region 2 in Figure 2.1), respectively. WD, TD and ND correspond to welding, transversal and normal directions, respectively.

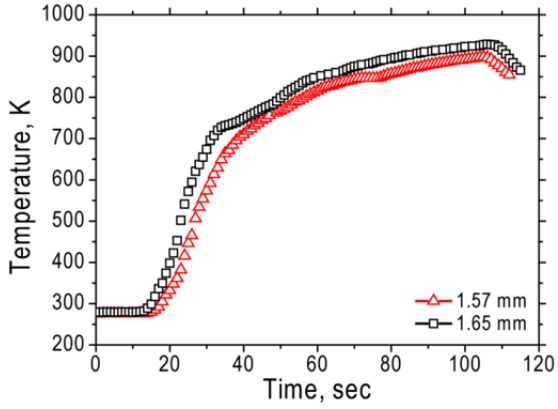

(a)

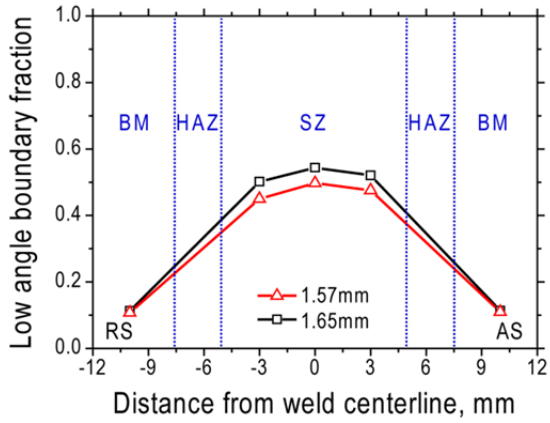

(b)

Figure 2.3 (a) Temperature-time profiles measured at the root of tool shoulder and (b) profiles of LAB fraction for the two welded samples with two different plunging depths of 1.57 and 1.65 mm as a function of the distance from the weld centerline. RS and AS indicate retreating and advancing sides, respectively.

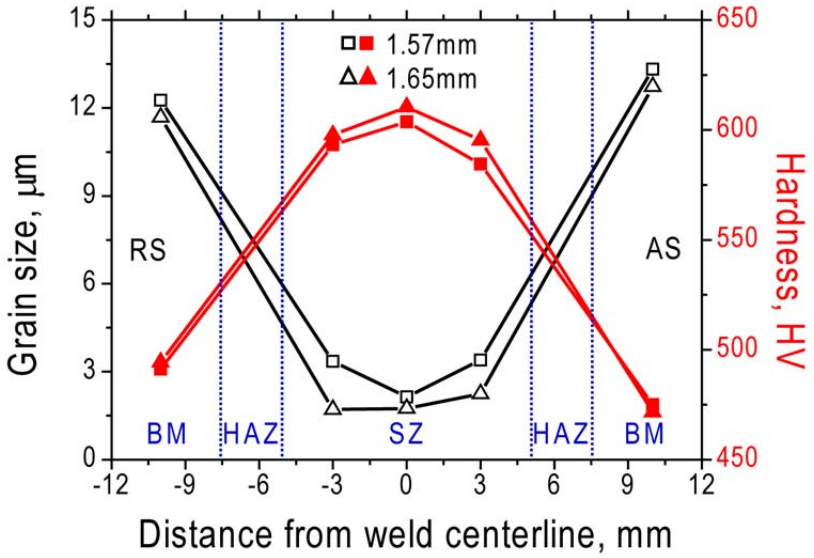

Figure 2.4 Profiles of grain size and hardness for the two welded samples with two different plunging depths of 1.57 and 1.65 mm as a function of the distance from the weld centerline. Grain size and hardness profiles were depicted as black and red lines, respectively. RS and AS indicate retreating and advancing sides, respectively.

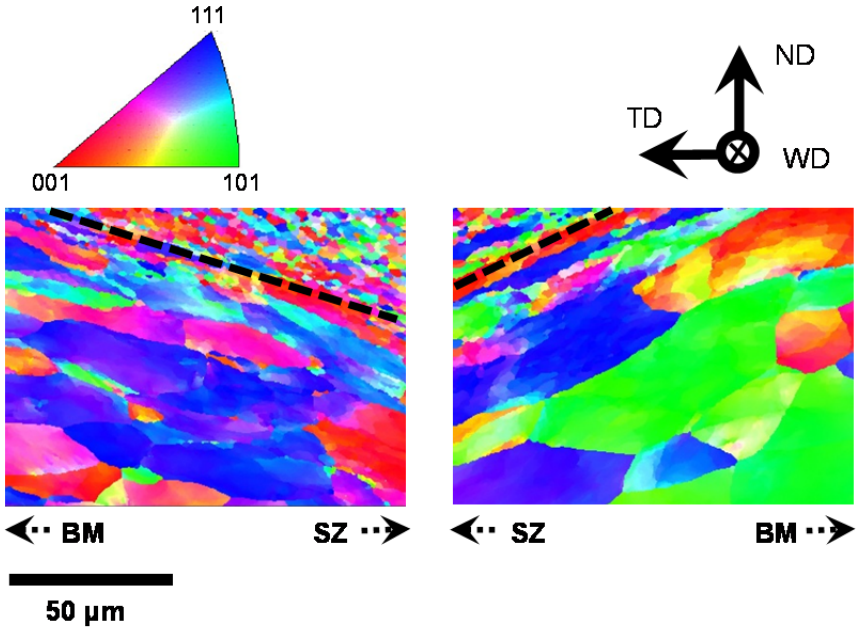

(a) (b)

Figure 2.5 Orientation maps of TMAZ on the (a) RS and (b) AS, respectively.

2.4 Conclusion: Steel without phase transformation

This present study examined the microstructure and hardness of FSW joints of 409 ferritic SS. High-quality, defect-free welds were successfully produced in the ferritic SS by FSW using a PCBN tool at a tool rotation speed of 600 rpm and a welding speed of 254 mm/min. A remarkably fine-grained microstructure was obtained in the SZ by dynamic recrystallization due to severe shear deformation and high heat generated during FSW process. The resulting smaller grains increased the hardness of the SZ. The fraction of LAB in the SZ was significantly increased as compared to that in the BM, and the texture in the SZ was very close to a shear texture in bcc materials. Lastly, the increase in plunging depth increased the amounts of both heat input and plastic deformation to the welded material during FSW, which led to an increase in the fraction of LAB, a decrease in the grain size, and an increase in the hardness in the SZ.

2.5 References

[1] Sato YS, Urata M, Kokawa H, Ikeda K, Enomoto M. Scripta Mater 2001;45:109.

[2] Sato YS, Kurihara Y, Park SHC, Kokawa H, Tsuji N. Scripta Mater 2004;50:57.

[3] Reynolds AP, Tang W, Gnaupel-Herold T, Prask H. Scripta Mater 2003;48:1289.

[4] Sato YS, Nelson TW, Sterling CJ. Acta Mater 2005;53:637.

[5] Sato YS, Nelson TW, Sterling CJ, Steel RJ, Pettersson CO. Mater Sci Eng A 2005;397:376.

[6] Fujii H, Cui L, Tsuji N, Maeda M, Nakata K, Nogi K. Mater Sci Eng A 2006;429:50.

[7] Sato YS, Yamanoi H, Kokawa H, Furuhara T. Scripta Mater 2007;57:557.

[8] Thomas WM, Threadgill PL, Nicholas ED. Sci Technol Weld Joi 1999;4:365.

[9] Okamoto K, Hirano S, Inagaki M, Park SHC, Sato YS, Kokawa H, Nelson TW, Sorensen CD. Proceedings of Fourth International Symposium on Friction Stir Welding. 2003.

[10] Humphreys FJ, Hatherly M. Recrystallization and Related Annealing Phenomena, second ed.. Oxford: Elsevier, 2004.

[11] Schramm RE, Reed RP. Metall Mater Trans A 1975;6A:1345.

[12] Vecchio KS, Hertzberg RW. J Mater Sci 1988;23:2220.

[13] Kang SH, Bang WH, Cho JH, Han HN, Oh KH, Lee CG, Kim SJ. Mater Sci Forum 2005;495:901.

[14] Kang SH, Han HN, Oh KH, Cho JH, Lee CG, Kim SJ. Met Mater Int 2009;15:1027.

[15] Mironov S, Sato YS, Kokawa H. Acta Mater 2008;56:2602.

[16] Hurley PJ, Humphreys FJ. Acta Mater 2003;51:1087.

[17] Cho JH, Kang SH, Han HN, Oh KH. Met Mater Int 2008;14:247.

[18] Sato YS, Urata M, Kokawa H. Metall Mater Trans A 2002;33A:625.

Chapter 3

Numerical investigation on friction stir welding of steel without phase transformation

3.1 Introduction: Numerical approach

The heat transfer and material flow, which are the key parameters of FSW, vary according to the properties of welded material, the rotation and welding speeds of the tool, and the tool geometry. The complicated interactions among the various physical variables, which occur simultaneously, affect the heating/cooling rates, the material flow during FSW, and the microstructure and properties of the welded joints after FSW. Since its invention, the FSW method has been widely investigated to optimize the process and the relevant microstructure/properties of the joined material. Therefore, a fundamental knowledge for the complex physics during FSW should be required, and the rigorous numerical model coupled with experimental results is very suitable in this research.

Many attempts to develop numerical models coupled with experimental data have been reported. However, most of the early-developed models focused on heat transfer calculations and were indifferent to the material flow near the tool [1-5]. Frigaard et al. [1] developed a three-dimensional

numerical heat flow model for FSW based on a finite difference method. Their model was validated by in-situ thermocouple measurements and experimental hardness profiles measured at specific time intervals after FSW. Chao et al. [2] formulated a heat transfer problem during FSW by inverse modeling into two boundary value problems (BVP)-a steady BVP for the tool and a transient BVP for the workpiece-and solved the problem using a finite element method (FEM). They found that only 5% of the generated heat was transported into the tool and about 80% of the mechanical work was dissipated as heat. Song and Kovacevic [3,4] proposed a three-dimensional heat transfer model for FSW by adapting a moving coordinate. They concluded that preheating the workpiece is very beneficial to FSW. The temperatures computed using their model were in good agreement with the measured temperatures. Khandkar et al. [5] developed a three-dimensional thermal model to predict transient temperature distributions during FSW of aluminum alloys. The heat generation in their model was based on experimentally measured torque distributions. Good agreement between the simulated temperature profiles and experimental data was demonstrated by adjusting the bottom heat transfer coefficient. The various models mentioned above were very helpful for better understanding of FSW. However, those models disregarded convective heat transfer due to material flow during the process.

Several researchers have recently worked on the development of rigorous

numerical models considering convective heat transfer due to material flow during FSW. Cho et al. [6,7] used a two-dimensional heat and material flow model to predict the motion of material flow, thermal response, and strain hardening during FSW of 304L stainless steel. They used a simplified Hart's model [8] to calculate the flow stress and non-Newtonian viscosity. They found that temperature on the advancing side (AS) was about 100 K higher than that on the retreating side (RS). Texture evolution was also predicted from the computed velocity gradients along the streamline of the flow field. Seidel and Reynolds [9] developed a two-dimensional thermal model based on a laminar, viscous, and non-Newtonian flow around a circular cylinder. This model could not be directly used to validate experimental data such as forces on the pin, torque, and weld energy owing to the simplified assumptions. Ulysse [10] used a three-dimensional viscoplastic model to predict the temperature profile during FSW. Although there were discrepancies between computed and measured temperatures, this model enabled to predict changes of temperature profiles with welding variables. They also found that pin forces increase with increasing welding speeds, but the opposite effect was observed for increasing rotational speeds using parametric studies. Colegrove and Shercliff [11-13] developed a three-dimensional heat and material flow model during the FSW of aluminum alloys using a commercial computational fluid dynamics (CFD) code, FLUENT. They investigated changes of heat and material flow during FSW

with the design and rake angle of the tool through coupled thermal/flow analysis considering heat generation by viscous dissipation.

Nandan et al. reported results of a three-dimensional heat transfer and material flow during FSW of 6061 aluminum alloy [14], 304 austenitic stainless steel [15], and 1018 low carbon steel [16]. They examined the temperature fields, cooling rates, and plastic flow fields by solving the equations for conservation of mass, momentum and energy in three dimensions. They also considered heat generation, non-Newtonian viscosity as a function of strain rate and temperature, and temperature-dependent physical properties in the calculation. The computed temperatures were in good agreement with the corresponding experimentally determined values. Most recently, Guerdoux and Fourment [17] developed a three-dimensional numerical tool that allows computing the thermo-mechanical fields during all phases of FSW without any hypothesis or supplementary information about the process using an adaptive Lagrangian-Eulerian formulation based on accurate constitutive and friction models. Later, Assidi et al. [18] performed the calibration of friction model using the three-dimensional numerical results obtained with the developed arbitrary Lagrangian-Eulerian formulation. They reported that the Coulomb's friction model enables an excellent agreement with experimental results such as tool temperatures and forces. Also, Arora et al. [19] reported the computed strains and strain rates during FSW of 2524 aluminum alloy from a three-dimensional coupled viscoplastic flow and heat

transfer model. The computed strains and strain rates were in the ranges of -10 to 5 and -9 to 9 sec-1, respectively. Later, Arora et al. [20] proposed a well-tested analytical model enabling to predict velocities, peak temperature, and torque during FSW. However, these numerical studies have not focused on the changes of the microstructural characteristics such as the texture and the geometry of the FSWed region during/after the FSW process.

In the present study, a rigorous numerical model coupled and verified with both measured temperature histories and microstructural changes is developed based on a three-dimensional Eulerian finite volume (FV) method. Heat transfer, material flow, and texture development during FSW of 409 ferritic stainless steel are investigated using the developed model. Based on spatially variable thermo-physical properties such as density, thermal conductivity, specific heat capacity, and flow stress, and appropriate boundary conditions, a numerical solution procedure to examine the temperature change and material flow is incorporated into an implicit FV program. The model considers spatially variable heat generation rates and non-Newtonian viscosity as a function of local strain rate, temperature, and the characteristics of material. Also, the texture around the FSW tool is predicted from the computed velocity gradients along the streamlines of the flow field by using a visco-plastic self-consistent (VPSC) approach for polycrystal. To confirm the simulation results, the temperature histories during the FSW process and the microstructural changes after the FSW process are measured. The computed

temperatures, textures and viscosity contours are directly compared with the corresponding measured results.

3.2 Materials and experiments

In this study, FSW was applied on 409 stainless steel plates (bead on plate) with a convex scrolled shoulder tool made of polycrystalline cubic boron nitride (PCBN). The nominal chemical composition of the 409 stainless steel is listed in Table 3.1. The plates were 600 mm in length, 200 mm in width and 12 mm in thickness. The PCBN tool had a shoulder diameter of 36.8 mm at the root of the convex shoulder, a pin diameter of 5.7 mm, and a pin length of 1.2 mm. The thermo-physical properties of the stainless steel [21], and the welding parameters used in this study are listed in Tables 3.2 and 3.3, respectively. These data were used in the numerical simulation for FSW.

Thermocouples were instrumented to the plates to measure the temperature change during FSW. Figure 3.1 shows the bottom surface of a specimen plate and a schematic diagram of the thermocouple placements on a cross section perpendicular to the welding direction. Four R-type thermocouples (ch 1 to 4) were attached in 3 mm diameter holes drilled to a depth of 3 mm from the bottom plate after grooving to a depth of 2 mm, as shown in Figure 3.1b. The thermocouple lines protruded out of the workpiece along the groove. The thermocouples on channels 1, 2, and 3 recorded the temperature variations on AS, the center region, and RS around the SZ, respectively. The temperature changes on RS located a long way from the SZ were also measured at the thermocouple on channel 4. In addition, the

temperature of the tool during FSW was measured using a thermocouple inserted into the root of the tool shoulder through the tool holder.

In order to investigate the microstructure of the FSWed specimen, the plates were prepared perpendicular to the welding direction and examined by electron backscatter diffraction (EBSD: Oxford Inca system) equipped with a field emission scanning electron microscope (FE-SEM: JSM6500F). The samples were mechanically ground and electrolytically polished in a 90 ml ethanol + 10 ml perchloric acid solution at 20 V for 30 sec. Through the EBSD observation, the texture development in the SZ after FSW could be obtained.

Table 3.1 Chemical composition of 409 stainless steel.

Chemical compositions (wt. %)								
C	Cr	Fe	Mn	Ni	P	S	Si	Ti
≤ 0.08	11.13	86	≤ 1.0	≤ 0.5	≤ 0.045	0.030	≤ 1.0	0.75

Table 3.2 Thermo-physical properties of 409 stainless steel [21].

Temperature (K)	Density (kg/m^3)	Specific heat capacity (J/kg-K)	Thermal conductivity (W/m-K)
298	7800	-	-
373	7794	473	27.6
473	7786	515	27.6
673	7768	607	26.4
873	7749	-	25.1
1073	7730	691	-
1273	7712	-	21.8

Table 3.3 Process parameters for FSW and physical properties of PCBN tool.

Property/Welding parameter	Value
Welding speed	3 mm/s
Rotational speed	1400 rpm
Plunging depth	1.7 mm
Axial pressure, P_T	25.5 MPa
Tool material	PCBN
Density of tool	3120 kg/m^3
Thermal conductivity of tool	130 W/K
Specific heat capacity of tool	1966 J/kg-K

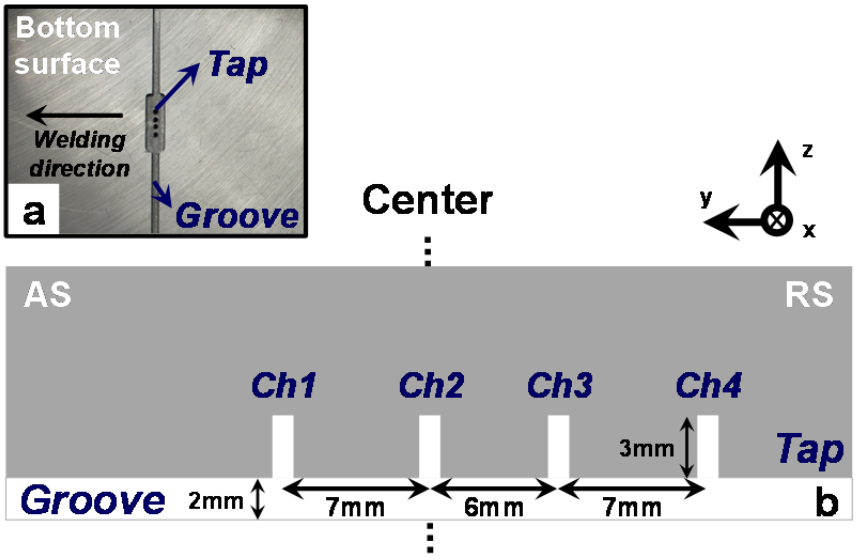

Figure 3.1 (a) Macrograph on bottom surface of specimen and (b) schematic diagram of thermocouple placements on cross section perpendicular to welding direction.

3.3 Numerical modeling: Governing equations and initial/boundary conditions

The FSW process consists of three subsequent procedures: plunging, dwelling, and pulling the tool out of the workpiece. During the dwelling period, the cylindrical tool shoulder rotates at a constant rotational speed with the tool pin completely inserted within the workpiece while the workpiece (or the tool) is translating against the tool (or the workpiece) along the welding direction at the constant welding speed. Thus, in contrast to the two other procedures, most of the heat is generated at a constant rate during the dwelling period, and the cross-sections of the welded specimen demonstrate similar geometry, microstructure, and properties, indicating a quasi-steady behavior [22]. In this study, partial sticking condition was assumed at the surface between the tool and the workpiece during the dwelling period. The tilt angle of the tool was taken as zero, and the tool shoulder was assumed to be flat.

The material during the FSW process was assumed to behave as an incompressible, single-phase flow. The continuity equation of the material can be written as:

$$\frac{\partial u_i}{\partial x_i} = 0 \tag{1}$$

where u is the velocity of material flow and i = 1, 2, and 3 which represent the *x*, *y*, and *z* directions shown in Fig. 1, respectively. The conservation of the momentum equation in index form can be given by [23]:

$$\frac{\partial \rho u_j}{\partial t} + u_i \frac{\partial \rho u_j}{\partial x_i} = -\frac{\partial P}{\partial x_j} + \frac{\partial}{\partial x_i}\left(\frac{\partial \mu u_j}{\partial x_i}\right) - \rho U_1 \frac{\partial u_j}{\partial x_1} \tag{2}$$

where ρ is the density, P is the pressure, μ is the non-Newtonian viscosity, and U_1 is the welding velocity. The term of $\frac{\partial \rho u_j}{\partial t}$ is set to zero when the momentum equation is solved for the steady flow. The calculation of viscosity needs the local values of strain rates and temperature. The viscosity is calculated based on the following formulation of flow stress, $\overline{\sigma}$, introduced by Sheppard and Wright [24] for the high strain-rate and large bulk deformation processes of metals:

$$\overline{\sigma} = \frac{1}{\alpha} \sinh^{-1}\left[\left(\frac{Z}{A}\right)^{1/n}\right] \tag{3}$$

where A, α, and n are material constants and Z is the Zener-Hollomon parameter. A, α, and n are obtained from open literature [25].

The Zener-Hollomon field variable incorporates the effect of the temperature and effective strain rate into the flow stress in the following equation:

$$Z = \dot{\varepsilon} \exp\left(\frac{Q}{RT}\right) \tag{4}$$

where R is the gas constant, Q is the temperature independent activation energy and $\dot{\varepsilon}$ is the effective strain rate. Q is obtained by minimizing the sum of the squared differences [26] between the ultimate tensile strength (UTS) data of the 409 stainless steel listed in Table 3.4 and calculated data. The optimized Q value is 49,809 J/mol-K.

Finally, viscosity can be calculated as a function of flow stress and effective strain rate using Perzyna's viscoplasticity model [27]:

$$\mu = \frac{\overline{\sigma}}{3\dot{\varepsilon}} \tag{5}$$

The above formulations were incorporated into a commercial code, FLUENT (ANSYS INC., USA), using a user defined function (UDF). The computed viscosity is dependent on both strain rate and temperature.

The thermal energy conservation equation can be written as:

$$\frac{\partial(\rho C_p T)}{\partial t} + u_i \frac{\partial}{\partial x_i}(\rho C_p T) = -\rho C_p U_1 \frac{\partial T}{\partial x_1} + \frac{\partial}{\partial x_i}\left(k \frac{\partial T}{\partial x_i}\right) + S_i + S_b \quad (6)$$

where C_p is the specific heat and k is the thermal conductivity. S_i represents the source term due to the interfacial heat generation rate per unit volume at the tool-workpiece interface and S_b is the heat generation rate due to plastic deformation in the workpiece away from the interface. These terms are described in the following section. In this equation, the time-dependent term of $\frac{\partial(\rho C_p T)}{\partial t}$ is zero when steady flow is assumed.

The initial temperature of the material flow and the air was assumed to be 298 K as shown in Figure 3.2. Initially, the material flows in and out of the inlet and outlet boundaries, respectively, at the welding speed of 3 mm/sec (the linear translation speed of the workpiece) as shown in Figure 3.2. On the other boundaries (sides, top, and bottom surfaces), except the boundary between the tool and the workpiece, a free traction boundary condition was applied. As mentioned above, the material was assumed to be in partial sticking with the tool, which rotated at the experimental rotation speed of 1400 rpm.

The heat generated at the interface between the vertical and horizontal surfaces of the tool and the workpiece, S_i, may be defined as [16]:

$$S_i = [(1-\delta)\eta\tau + \delta\mu_f P_N](\omega r - U_1 \sin\theta)\frac{A_r}{V} \quad (7)$$

where A_r is any small area on the tool-workpiece interface, r is the radial distance of the center of the area from the axis, V is the control-volume enclosing the area, A_r, τ is the maximum shear stress at yielding, θ is the angle with the negative *x*-axis in the counter-clockwise direction, η is the mechanical efficiency, i.e. the amount of mechanical energy converted to heat energy, δ is the spatially variable fractional slip between the tool and the workpiece interface, μ_f denotes the spatially variable coefficient of friction, ω is the angular velocity, and P_N is the normal pressure on the surface. The velocity $(\omega r - U_1 \sin\theta)$ represents the local velocity of a point on the tool with the origin fixed at the tool axis.

Mechanical efficiency, η, is assumed to be 0.5 guided by the range of the previous work in FSW [15,16,28]. In Eq. (7), when δ is 0, full sticking condition is applied and heat is generated only by plastic deformation, while all heat is generated by friction when δ is 1.

Fractional slip, δ, can be expressed by the following relation [16]:

$$\delta = 1 - \exp\left(-\frac{1}{\delta_0} \frac{\omega}{\omega_0} \frac{r}{R_S} \right) \tag{8}$$

where δ_0 is a constant, ω_0 is a constant to nondimensionalize the rotational speed of the tool, and R_S is the shoulder radius. This equation was determined from the reported experimental data of the tool-workpiece interfacial slip in a cross-wedge rolling process [29]. Figure 3.3a shows the variation of slip with radial distance. The value of δ_0 was taken as 0.4 [16].

The friction coefficient, μ_f, can be represented by the following form [16]:

$$\mu_f = \mu_0 \exp(-\lambda \delta \omega r) \tag{9}$$

where λ is a constant. The values of μ_0 and λ were taken as 0.4 and 1 s/m, respectively. This equation indicates that the friction coefficient is dependent on the relative velocity between the tool and the workpiece [30]. Figure 3.3b shows the variation of friction coefficient with radial distance from the tool axis.

The heat generated at the interface between the vertical and horizontal surfaces of the tool and the workpiece, S_i, may be defined as heat flux, q_1, and can be expressed as:

$$q_1 = [(1-\delta)\eta\tau + \delta\mu_f P_N](\omega r - U_1 \sin\theta) \quad \text{in the range} \quad r < R_P \qquad (10)$$

where R_P is the pin radius. At the shoulder-workpiece interface, a significant amount of heat will be transported to the tool material because the thermal conductivity of the tool material (PCBN) is approximately six times higher than that of the 409 stainless steel [16,31]. Thus, the rate of heat generation due to friction and plastic work at the shoulder-workpiece, q_2, may be written as:

$$q_2 = \frac{J_W}{J_W + J_T} q_1 \quad \text{in the range} \quad R_P \le r \le R_S \qquad (11)$$

$$J = \sqrt{k\rho C_p} \qquad (12)$$

where J represents the transported extent of heat generated at the shoulder-workpiece interface or the effusivity of the material. The subscripts *W* and *T*

denote the workpiece and the tool, respectively. Based on the data in Tables 3.2 and 3.3 at 1173 K, J_W is calculated as $J_W = 0.38 J_T$.

To be more specific, the J reprents the thermal inertia (or effusivity), which is a measure of material's ability to exchange thermal energy with its surroundings. At a one dimensional half-space, heat flow at the interface is proportional to the thrmal inetia based on the proper boundary conditions. Thus, we introduced the quantity to calculate the transported extent of heat generated at the shoulder-workpiece interface. Generally, the thermal diffusivity of a material is a measure of how fast the material temperature adapts to the surrounding temperature, and this value could not be applicable to this case.

Convective and radiative heat transfer coefficients were used for the top surface of the workpiece as the following form:

$$-k\frac{\partial T}{\partial z}\bigg|_{top} = \sigma\varepsilon(T^4 - T_a^4) + h_t(T - T_a) \tag{13}$$

where σ is the Stefan-Boltzmann constant, ε is the external emissivity, and h_t is the heat transfer coefficient of 30 W/m^2-K. At the bottom surface, due to the intimate contact of the workpiece with the backing plate, the heat transfer coefficient of 50 W/m^2-K was used:

$$k\left.\frac{\partial T}{\partial z}\right|_{bottom} = h_b(T - T_a) \tag{14}$$

At the side surface of the workpiece, the convective heat transfer coefficient of 30 W/m^2-K was used.

A value of the viscous dissipation of momentum per unit volume, S_b, has been calculated as $f_m \mu \Phi$, where Φ is given by [16]:

$$\begin{aligned}\Phi = 2&\left(\left(\frac{\partial u_1}{\partial x_1}\right)^2 + \left(\frac{\partial u_2}{\partial x_2}\right)^2 + \left(\frac{\partial u_3}{\partial x_3}\right)^2\right) \\ &+ \left(\frac{\partial u_1}{\partial x_2} + \frac{\partial u_2}{\partial x_1}\right)^2 + \left(\frac{\partial u_1}{\partial x_3} + \frac{\partial u_3}{\partial x_1}\right)^2 + \left(\frac{\partial u_3}{\partial x_2} + \frac{\partial u_2}{\partial x_3}\right)^2\end{aligned} \tag{15}$$

and f_m is an arbitrary constant that indicates the extent of atomic mixing in the system. In this study, a value of 0.05 was used because this value resulted in the viscous dissipation of about 4% of the total heat generation for the welding conditions investigated [16].

Table 3.4 Ultimate tensile strength (UTS) data of 409 stainless steel.

Strain rate (/sec)	Temperature (K)	UTS (MPa)
0.3	973	175
0.3	1173	39
1.2	973	197
1.2	1173	49

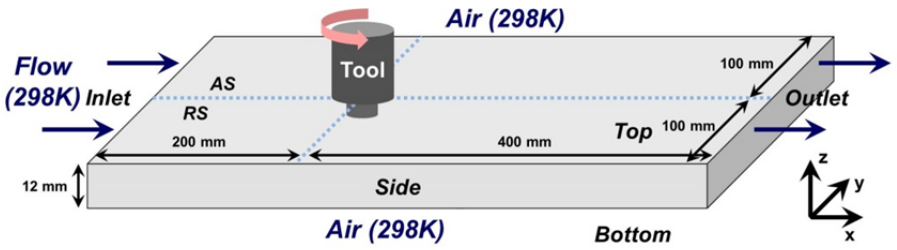

Figure 3.2 Dimensions of workpiece: a schematic view of the thermo-mechanical model.

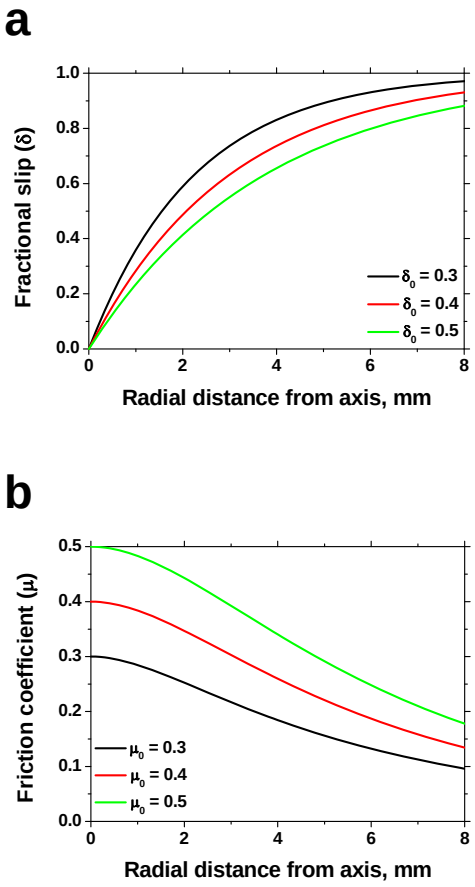

Figure 3.3 Variations of (a) fractional slip (δ) and (b) friction coefficient (μ) with radial distance from the tool axis for different scaling constants. For (b), δ_0 was fixed at 0.4.

3.4 Model description

Thermo-mechanical simulation of the FSW process for the 409 stainless steel sheet was performed using the computational fluid dynamics (CFD) code, Fluent 6.3.26 (ANSYS INC., USA) based on the governing equations and the boundary conditions as mentioned above. Conservation principles of mass, momentum, and energy were calculated considering the continuity equation for the incompressible single-phase flow. At steady state, the single-phase conservation of momentum and the conservation of thermal energy were solved assuming the partial stick condition between the viscoplastic material and the FSW tool.

The whole process consists of a rotating tool and moving workpiece, as shown in Figure 3.2. The dimensions of the 409 stainless steel sheet (workpiece) are 200 mm × 600 mm × 12 mm as shown in Figure 3.2. Also, the simplified cylindrical tool was used in the numerical model considering the tool geometry and the plunging depth as listed in Table 3.3 [3,32]. If it is assumed that the pin diameter and the pin length used in the numerical model are equal to the pin diameter of PCBN tool and the plunging depth, respectively, the shoulder diameter could be determined from both the cross-sectional macrograph of the welded sample [33] and the plunging depth. Thus, the shoulder diameter, the pin length, and the pin diameter of the simplified cylindrical tool used in the numerical studies are 15 mm, 1.7 mm and 5.7 mm,

respectively. The welding conditions are the same as the experimental conditions. Figure 3.4 shows a total of 356,862 hexahedral mesh elements, which typically have an average of 14 cell faces. The design and number of mesh elements are determined considering both the efficiency and accuracy of the computation.

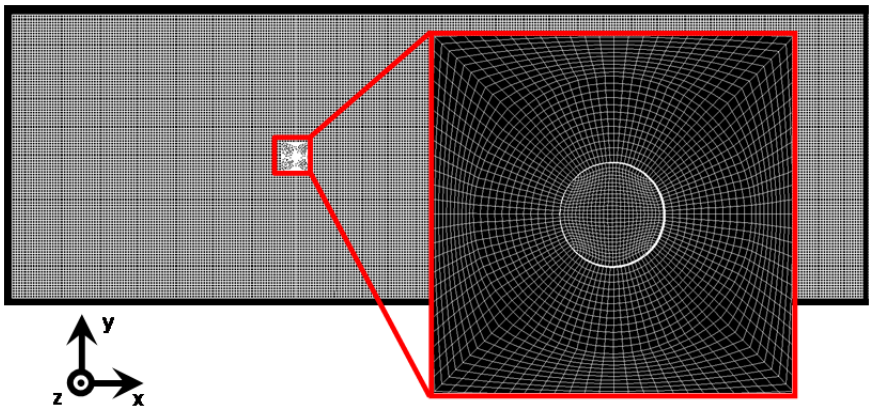

Figure 3.4 Top views of mesh system for finite volume calculation.

3.5 Prediction of texture evolution

Rapid changes in the microstructural characteristics during FSW process cause significant texture evolution, which depends on the thermo-mechanical history of the material. Texture evolution could be computed using a well-established framework based on polycrystal plasticity (VPSC code) [34,35]. The essential equations are summarized here. The velocity of a material particle, u, in a flow field described by an Eulerian reference frame is given by:

$$u_i = \frac{\partial x_i}{\partial t} \tag{16}$$

where x is the position of the material particle and t represents time. The velocity gradient, L, is obtained by taking the spatial gradient of the velocity field:

$$L = \frac{\partial u_i}{\partial x_j} \tag{17}$$

This motion at the macroscopic scale is linked to the crystal scale by adopting the extended Taylor hypothesis [36] such that individual crystals are assumed to undergo the macroscopic velocity gradient. In the case of the high

symmetry crystals and large strains considered here, this approximation is reasonable. Since elastic effects are neglected and crystals are assumed to deform solely by crystallographic slip, the crystal velocity gradient can be decomposed into a shearing along slip systems and a rigid lattice rotation:

$$L = L^C = \Omega + \sum_\alpha \dot{\gamma}^\alpha T^\alpha \tag{18}$$

where Ω is the lattice spin, $\dot{\gamma}^\alpha$ is the shear strain rate on the slip system α, and T^α is the Schmid factor. Here, $T^\alpha = b^\alpha \otimes n^\alpha$, with b^α, the slip direction, and n^α, the slip plane normal for slip system α. A viscoplastic constitutive relation is used to relate the shear strain rate on a slip system to the resolved shear stress [37]:

$$\dot{\gamma}^\alpha = \dot{\gamma}_0 \frac{\tau^\alpha}{\hat{\tau}} \left| \frac{\tau^\alpha}{\hat{\tau}} \right|^{(1/m-1)} \tag{19}$$

where m is the rate sensitivity, $\hat{\tau}$ is the slip system hardness (assumed to be identical for all slip systems), and $\dot{\gamma}_0$ is a reference strain rate. The values of m, $\hat{\tau}$, and $\dot{\gamma}_0$ are 0.05, 10 MPa, and 0.001 for {110}〈111〉 and {112}〈111〉 slip systems, respectively. The resolved shear stress on the slip

system α is obtained as the projection of the crystal stress onto the slip system:

$$\tau^{\alpha} = P^{\alpha} \cdot \sigma^{C'} \tag{20}$$

where $P^{\alpha} = symT^{\alpha}$ and $\sigma^{C'}$ is the deviatoric crystal stress. An expression for the crystal stress follows by combining the symmetric part of the crystal velocity gradient in Eq. (18) with Eqs. (19) and (20):

$$\sigma^{C'} = C^{C}[D^{C'}] \tag{21}$$

where the stiffness C^{C} is defined as

$$C^{C-1} = \sum_{\alpha} \frac{\dot{\gamma}_0}{\hat{\tau}^{\alpha}} \left| \frac{\tau^{\alpha}}{\hat{\tau}^{\alpha}} \right|^{(1/m-1)} P^{\alpha} \otimes P^{\alpha} \tag{22}$$

and $D^{C'}$ is the crystal deviatoric deformation rate. The skew part of the crystal velocity gradient in Eq. (18) yields an expression for the lattice spin:

$$\Omega = W - \sum_{\alpha} \dot{\gamma}^{\alpha} Q^{\alpha} \tag{23}$$

where W is the macroscopic spin, and $Q^{\alpha} = skewT^{\alpha}$.

3.6 Thermo/mechanical behavior of steel without phase transformation

The FSW process is simulated with the model equations and numerical algorithms presented in the previous sections. The computed temperature profiles along the longitudinal section around the tool and on the top surface of the workpiece are shown in Figure 3.5a and b, respectively. The temperature profiles on the longitudinal midsection (Figure 3.5a) and on the top surface of the workpiece (Figure 3.5b) are compressed in the front of the tool and are expanded behind the tool. The computed peak temperature is 1028 K. The computed results demonstrate that heat is supplied rapidly to the cold region of the workpiece ahead of the tool while heat is transported at a slower rate to the material already preheated behind the tool due to the low diffusivity of the material. This asymmetry becomes more prominent at high welding speeds, and the computed temperature profiles on the top surface with various welding speeds (Figure 3.5b and Figure 3.6a and b) describe well this tendency. Figure 3.5b and Figure 3.6a and b show that the welding speed is strongly related to the distribution speed of the heat into the trailing direction. Thus, the temperature distribution in Figure 3.6b with highest welding speed is thinner and longer than other temperature distributions.

Also, asymmetric temperature distribution is observed along the white dotted line in Figure 3.5a. Generally, the AS has higher shearing rate than the

RS, considering the direction of the material flow relative to the tool rotation. Thus, greater heat dissipation occurs along the AS than the RS. This phenomenon can be well explained from the forms of streamlines around the tool computed using the numerical model [6]. Figure 3.7 shows the computed temperature distribution along the white dotted line (z = 6 mm) in Figure 3.5a. As shown in Figure 3.7, the temperature is slightly higher on the AS than the RS, and this result is in agreement with the literature [6,38]. The relatively high temperature also lowers the flow stress and the strength of the material during the FSW process, and consequently the temperature difference would affect the difference of the hardness on the AS and the RS after the FSW process [6].

Thermal histories were constructed from the steady state temperature distribution by converting the distance traveled by the tool pin to the time using welding speed [16,39]. The computed thermal histories at the thermocouple locations described in Figure 3.1b agree reasonably well with the measured thermal histories as illustrated in Figure 3.8. The results show that temperature increases rapidly during heating and decreases slowly during cooling. This behavior could be consistent with the asymmetric temperature distribution along the welding direction observed in Figure 3.5b. In other words, the initial rapid heating and comparatively slower cooling encounter the compressed thermal contours ahead of the tool and the expanded temperature contours behind of the tool, respectively. The computed results

matched reasonably well with the experimental data, and this good agreement indicates that the model can be used to predict temperature profiles and histories during FSW.

It is well known that a significant amount of heat is generated at the interface between the tool and the workpiece during the FSW process due to intense friction and severe plastic deformation. Since the heat varies with the extent of friction and mechanical efficiency value, the sensitivity of the peak temperature on the above variables was examined. It is observed that the peak temperature increases as the friction coefficient (Figure 3.9a) and mechanical efficiency (Figure 3.9b) increase, respectively. The mechanical efficiency is the extent of transforming the mechanical work into the heat. The results demonstrate that the peak temperature is sensitive to both the extent of friction and mechanical efficiency. Once again, note that the value of δ_0 was taken as 0.4 [16].

The computed effective strain rate histories at the above-mentioned monitoring locations suggest that the effective strain rate increases rapidly in the vicinity of the tool where severe shear deformation occurs by friction stirring as shown in Figure 3.10. The severe shear deformation is one of the main factors which cause the significant microstructural changes during the FSW process. The maximum effective strain rate is higher at closer to the weld center. In other words, the maximum effective strain rate computed at

channel 2 (center region) is highest. The maximum value among the computed effective strain rates at the four monitoring locations is 33 sec^{-1} and this value is approximately consistent with other reported results [16,19,38].

An important result is that the viscosity can be very useful for predicting the geometry of the thermomechanically affected zone (TMAZ), which is an important factor to determine the properties of the weld. Figure 3.11 shows a comparison of the cross sections of the weld and the computed viscosity contours during FSW with the identical process parameters (rotation speed of 1400 rpm and welding speed of 3 mm/sec). The figure shows that the morphology of the computed viscosity contour is approximately similar to that of the FSWed region. The viscosity in the SZ, where strong material flow occurs during FSW, is much lower than that in the TMAZ. Thus, the viscosity changes drastically in the vicinity of the boundary between the SZ and TMAZ. This result means that SZ and TMAZ of FSW joints can be predicted by numerical analysis, which is a relatively simple and inexpensive method compared with the experimental method. The order of magnitude of non-Newtonian viscosity is consistent with the value usually observed in typical viscoplastic processing of materials such as extrusion [40].

The orientation map in Figure 3.12 illustrates significant microstructural change in the vicinity of the boundary between the SZ and the TMAZ on the RS (marked as a red rectangle in Figure 3.11a). The low-angle boundaries (2^o<LABs<15^o) and the high-angle boundaries (HABs>15^o) are depicted as

white and black lines, respectively. The fine-grained microstructure is observed in the SZ since continuous dynamic recrystallization occurs by the substantial shear deformation and significant amount of heat generated during FSW [33], comparing with the other region. Also, many low-angle boundaries are distributed within the large grains in the TMAZ due to the thermo-mechanical effect derived from SZ during FSW. The results shown in Figure 3.11 and Figure 3.12 confirm that the change of the microstructural characteristics in the vicinity of the boundary between the SZ and the TMAZ is closely related to that of the viscosity, which is a main factor to determine whether the material flow occurs or not.

Figure 3.13 shows the stream trace for flow number around the tool. The lines show the paths of which the material particles flow from the inlet to the outlet as shown in Figure 3.2. The results show that the streamlines have almost straight paths in the region located some distance from the tool. However, around the tool, the streamlines are nearly circular, closed forms, and plastic flows recirculate around the tool pin. Also, the results show that streamlines occupy larger areas at higher elevations due to the greater momentum transporting from the rotating shoulder. Thus, the SZ, where material flow occurs, has a basin-like shape which widens considerably towards the upper surface as shown in Figure 3.11. In addition, the streamlines around the tool indicate that material transfer occurs mainly on the RS, and consequently, a relative stagnation zone (a zone with zero-valued

velocity) exists in the RS of the tool as shown in Figure 3.13. The difference of the material flow is closely related to that of the temperature on the AS and the RS as shown in Figure 3.7. This result is in agreement with the open literature [6,9,16]. As a result, the computed streamlines demonstrate that the material flow generated during FSW can significantly affect the change of the microstructural characteristics such as the geometry of the FSWed region and the strength.

Polycrystal aggregates with 1000 discrete crystals are used to predict texture evolution during the FSW process. These single crystal aggregates are chosen initially from a uniform distribution. The texture evolution can be investigated by extracting the velocity gradients along the streamlines and using the velocity gradients as input to the VPSC code. As stated previously [33,41,42], FSW processes involve significant shearing of the material. In general, shear deformation occurs by glide on {110}, {112}, {123} planes in the <111> direction in α-Fe that results in the typical shear texture components [33,41].

{110} pole figures were calculated along streamlines around the tool and at some distance from the tool. Also for comparison, {110} pole figures were measured at the SZ and the base material. The pole figure along the streamline around the tool (Figure 3.14a) is identical to the typical shear texture components measured at the SZ (Figure 3.14c), although the major texture components are slightly rotated relative to a shear plane and shear direction.

The result confirms that the shear deformation is a major deformation mode that occurs in the vicinity of the tool during the FSW process. Also, the shear texture might weaken gradually with distance from the tool axis to the shoulder periphery. Beyond the periphery, the shear texture would weaken sharply due to the rapid decrease of shear deformation and consequently, change into a random texture as shown in Figure 3.14b and d. The computed results are well consistent with experimental results, and this good agreement indicates that the model can be used to predict texture evolutions during the FSW process.

As mentioned above, considerably fine homogeneous grains developed in the SZ due to the continuous dynamic recrystallization. In the SZ, the average grain size is about 6.26 μm, which is approximately seven times smaller than that of the base material as shown in the orientation maps in Figure 3.15a-(i) and b-(i). The grain size was measured by linear interception. The grain boundaries of the base material are composed of mostly high-angle boundaries and only a few low-angle boundaries. Misorientation-angle distribution in the base material is very close to a random distribution, which is shown as the dotted line in Figure 3.15b-(ii). In contrast, as shown in Figure 3.15a-(ii), the fraction of low-angle boundaries in the SZ (about 43.6%) is significantly larger than that in the base material (about 10.8%). This indicates that not only dynamic recrystallization but also recovery occurred in the SZ during the FSW process due to the significantly increased temperature of the

material [33]. As a result, severe shear deformation and high heat generated during the FSW process can cause significant microstructural changes as shown in Figure 3.15, and these changes can be explained from the temperature, material flow, and texture computed using the rigorous numerical model.

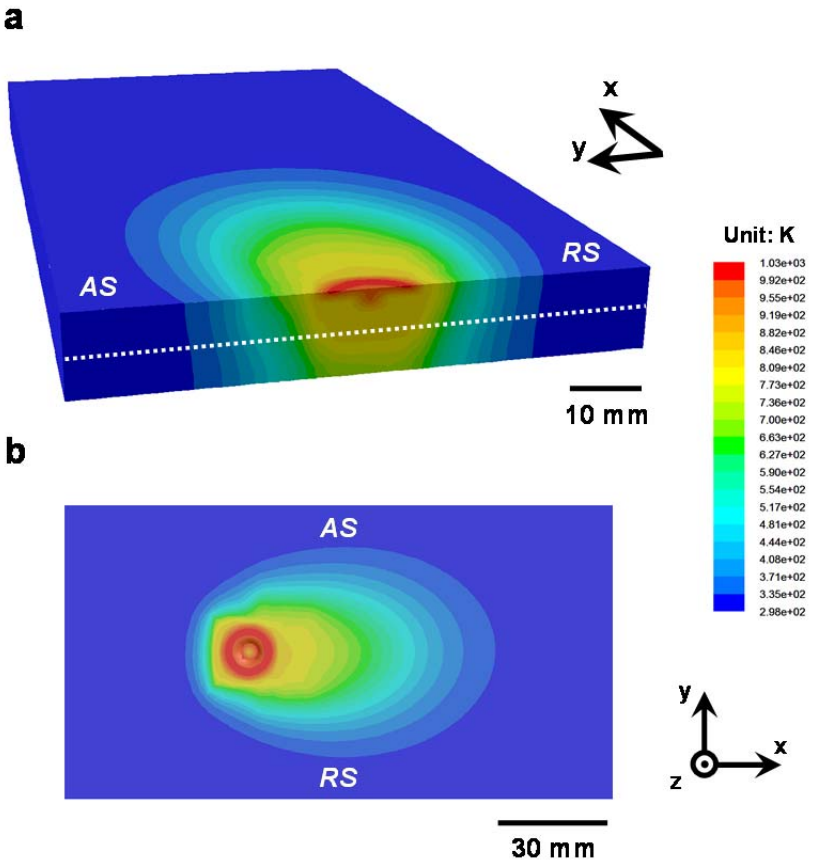

Figure 3.5 Computed temperature profiles in (a) x = 2.85 mm (yz-plane, xy-plane) and (b) z = 12 mm (the top surface of the workpiece) for the welding condition of 1400 rpm and 3 mm/sec.

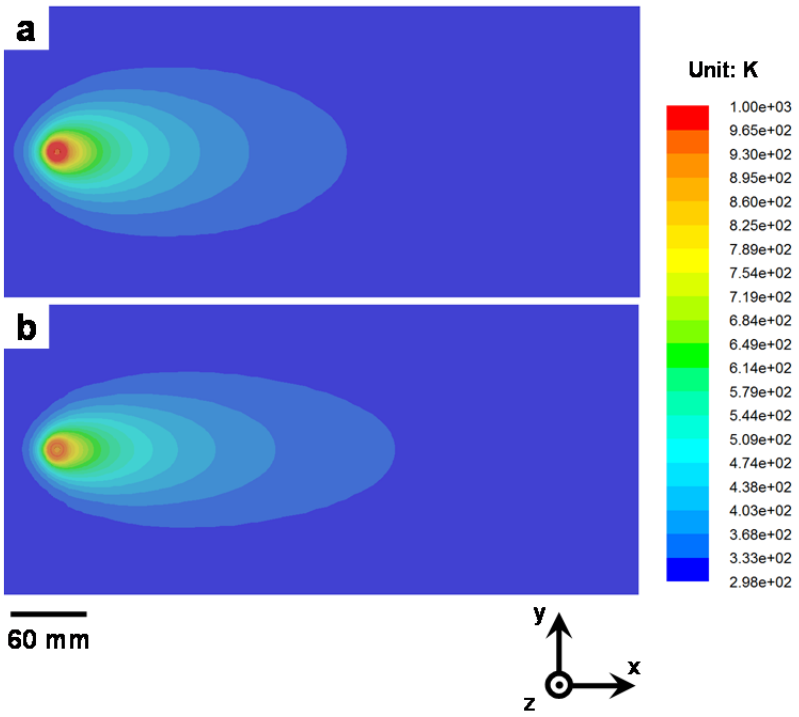

Figure 3.6 Computed temperature profiles on the top surface of the workpiece for the welding condition of (a) 1400 rpm and 6 mm/sec, (b) 1400 rpm and 9 mm/sec.

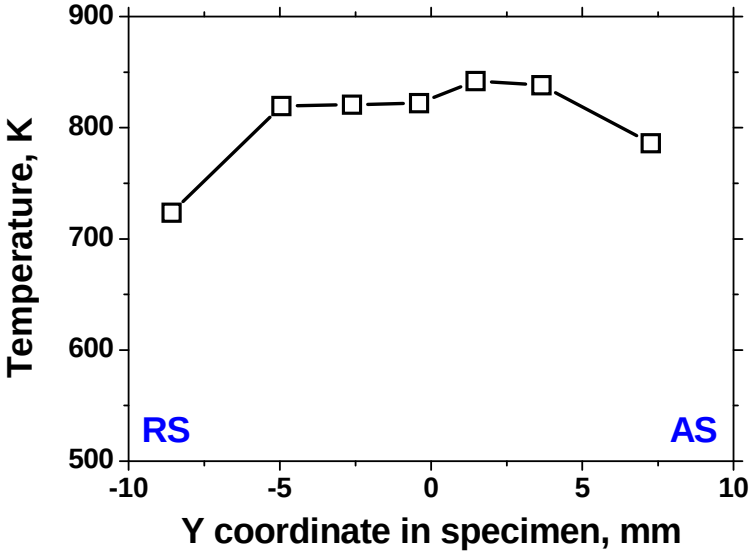

Figure 3.7 Variation of computed temperature along the white dotted line (z = 6 mm) in Figure 3.5a.

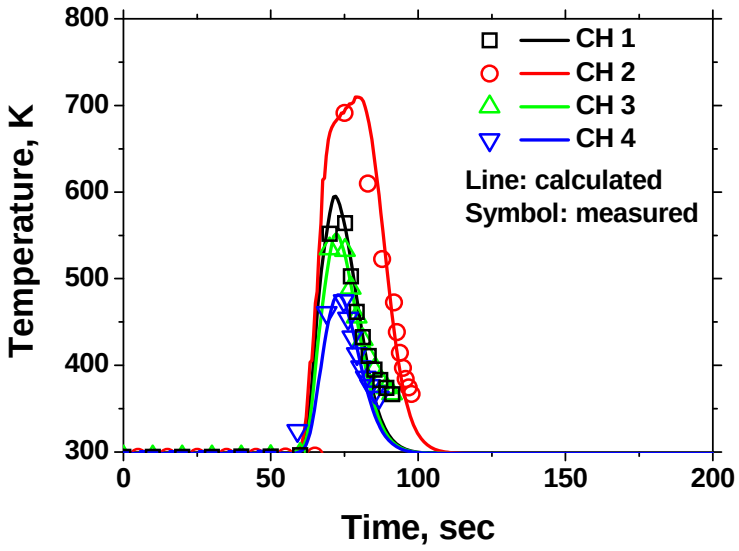

Figure 3.8 Comparison between the calculated and measured time-temperature profiles at the several locations, which are 3 mm from the bottom place after grooving to a depth of 2 mm and at -7, 0, 6, 13 mm away from the welding center. *Note*: See CH 1~4 in Figure 3.1.

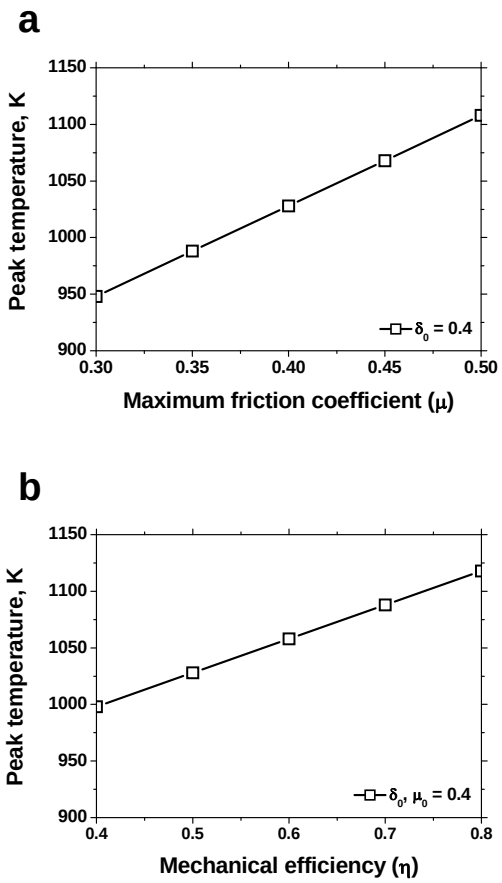

Figure 3.9 Variations of the computed peak temperature in the workpiece with (a) friction coefficient and (b) mechanical efficiency factor.

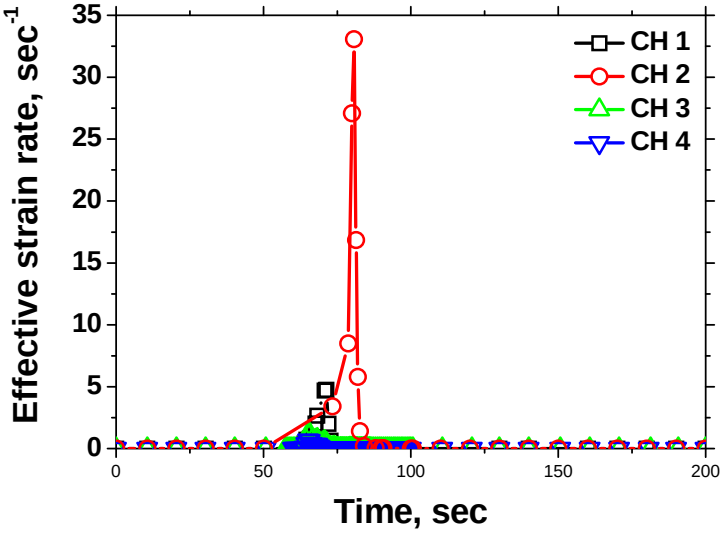

Figure 3.10 Computed effective strain rate histories at several monitoring locations, which are 3 mm from the bottom place after grooving to a depth of 2 mm and at -7, 0, 6, 13 mm away from the welding center. *Note*: See CH 1~4 in Figure 3.1.

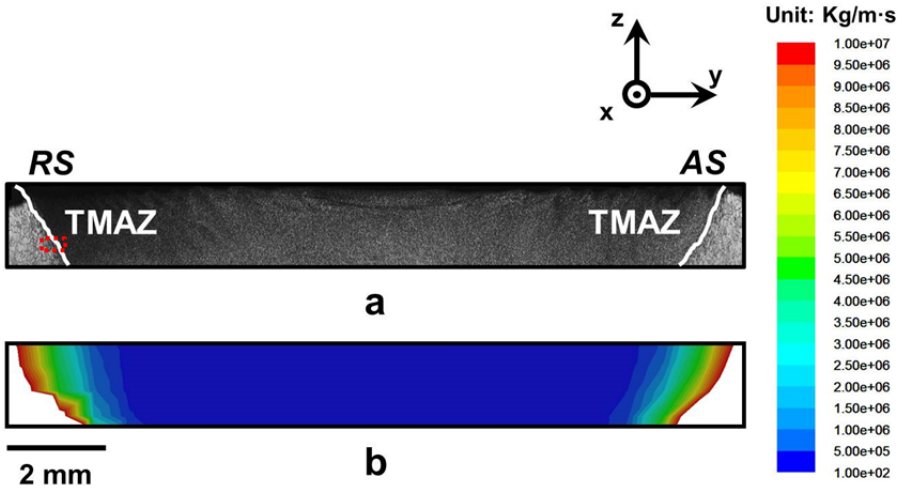

Figure 3.11 Comparison of the cross sections of (a) the weld and (b) the computed viscosity contours during FSW with the identical process parameters. The white line means approximate TMAZ.

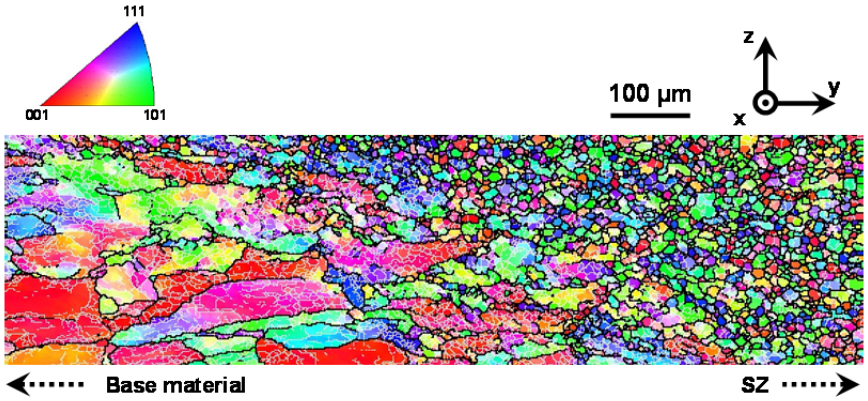

Figure 3.12 Orientation map in the vicinity of the boundary between SZ and TMAZ on the RS (marked as a red rectangle in Figure 3.11a).

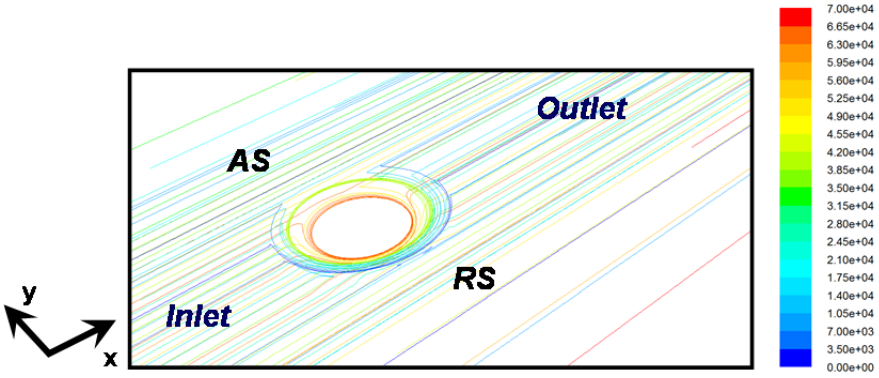

Figure 3.13 Stream trace for flow number around the tool.

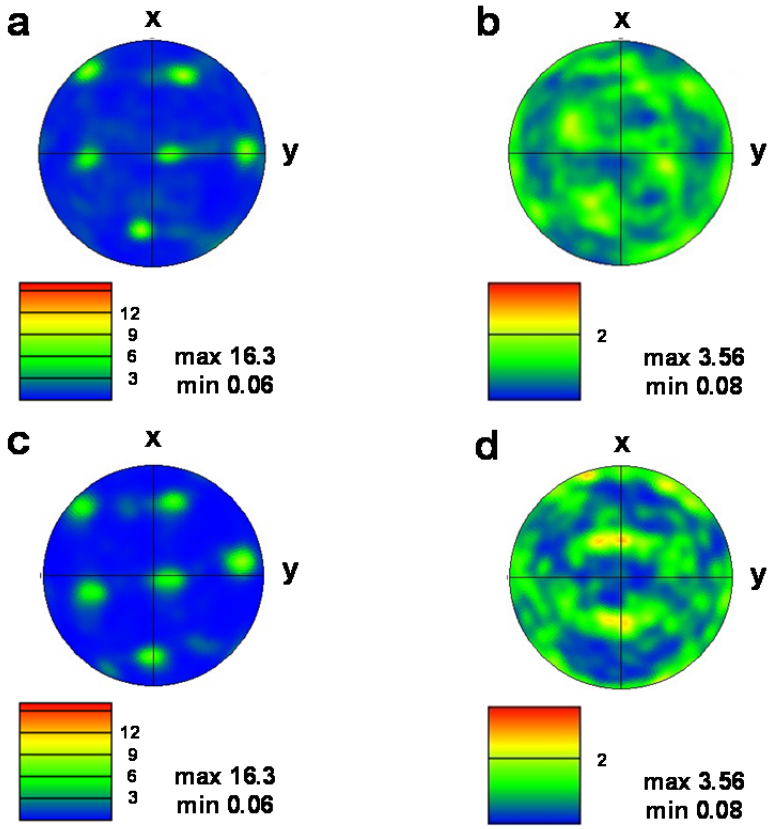

Figure 3.14 {110} pole figures calculated along (a) streamline around the tool and (b) streamline far away from the tool in Figure 3.13 and measured at (c) SZ and (d) base material.

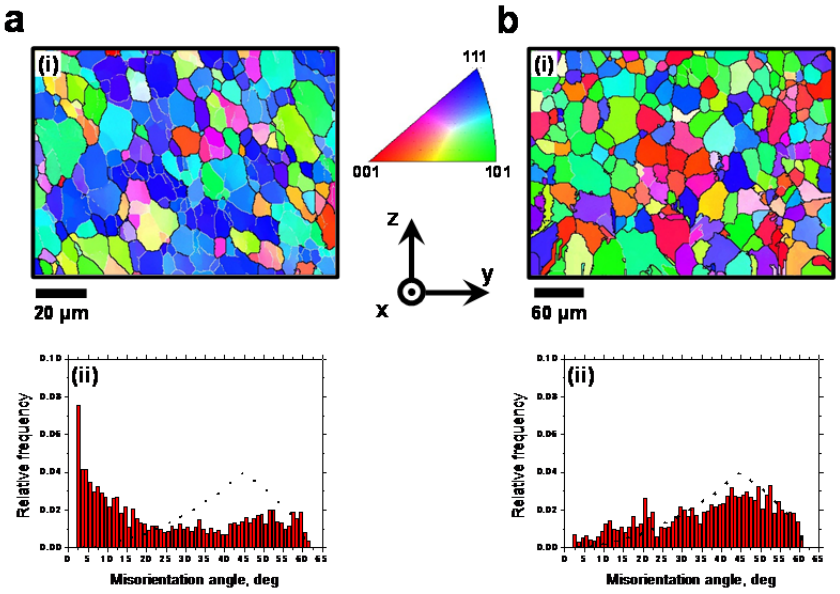

Figure 3.15 (i) Orientation map and (ii) misorientation-angle distribution (random distribution is shown by a dotted line) of (a) SZ and (b) base material, respectively.

3.7 Conclusion: Numerical approach

Three-dimensional heat transfer and material flow during the FSW of 409 ferritic stainless steel have been computed by solving the governing equations of mass, momentum, and energy using temperature-dependent physical properties. The non-Newtonian viscosity was determined from the computed values of strain rate, temperature and material properties. The computed results show that temperature increases rapidly around the tool mainly due to the heat generated at the interface between the tool and the workpiece. The computed results also show typical asymmetric temperature distribution along the welding and transverse directions due to the rotational and linear motion of the tool. This asymmetric behavior becomes more prominent as the welding speed increases. The computed effective strain rate increases rapidly around the tool, where severe shear deformation occurs by intense friction stirring. In contrast, the computed viscosity decreases rapidly around the tool, where the flux of the material occurs. The computed temperature histories agreed well with the experimental results, and the morphology of the computed viscosity contour was identical to that of the real FSWed region. The computed streamlines indicate that the streamlines around the tool are nearly circular, closed forms. Also, the computed streamlines illustrate that the material flow occurs mainly on the RS of the tool. The texture around the FSW tool was predicted from the computed velocity

gradients along the streamlines of the flow field. The shear deformation texture was significantly developed around the tool, and the computed texture agreed fairly well with the experimental data. A remarkably fine-grained microstructure was obtained in the SZ by continuous dynamic recrystallization due to the severe shear deformation and high heat generated during the FSW process. The fraction of LAB in the SZ was significantly increased compared to that in the base material. Finally, it was confirmed that the changes of the microstructural characteristics during/after the FSW process are closely related to those of the temperature, strain rate, viscosity, material flow and texture computed using the numerical model. Although some assumptions required in the numerical model could be weaknesses of the model or cause uncertainty of the computed results, the presented studies demonstrated sufficient possibilities, which can predict directly the changes of microstructural characteristics during the FSW process by using the rigorous numerical model.

3.8 References

[1] Frigaard O, Grong O, Midling OT. Metall Mater Trans A 2001;32:1189.

[2] Chao YJ, Qi X, Tang W. J Manuf Sci E-T Asme 2003;125:138.

[3] Song M, Kovacevic R. Int J Mach Tool Manu 2003;43:605.

[4] Song M, Kovacevic R. P I Mech Eng B-J Eng 2004;218:17.

[5] Khandkar MZH, Khan JA, Reynolds AP. Sci Technol Weld Joi 2003;8:165.

[6] Cho JH, Boyce DE, Dawson PR. Mat Sci Eng a-Struct 2005;398:146.

[7] Cho JH, Dawson PR. Metall Mater Trans A 2006;37A:1147.

[8] Hart EW. J Eng Mater-T Asme 1976;98:193.

[9] Seidel TU, Reynolds AP. Sci Technol Weld Joi 2003;8:175.

[10] Ulysse P. Int J Mach Tool Manu 2002;42:1549.

[11] Colegrove PA, Shercliff HR. Sci Technol Weld Joi 2004;9:345.

[12] Colegrove PA, Shercliff HR. Sci Technol Weld Joi 2004;9:352.

[13] Colegrove PA, Shercliff HR. J Mater Process Tech 2005;169:320.

[14] Nandan R, Roy GG, Debroy T. Metall Mater Trans A 2006;37A:1247.

[15] Nandan R, Roy GG, Lienert TJ, DebRoy T. Sci Technol Weld Joi 2006;11:526.

[16] Nandan R, Roy GG, Lienert TJ, Debroy T. Acta Mater 2007;55:883.

[17] Guerdoux S, Fourment L. Model Simul Mater Sc 2009;17.

[18] Assidi M, Fourment L, Guerdoux S, Nelson T. Int J Mach Tool Manu 2010;50:143.

[19] Arora A, Zhang Z, De A, DebRoy T. Scripta Mater 2009;61:863.

[20] Arora A, DebRoy T, Bhadeshia HKDH. Acta Mater 2011;59:2020.

[21] Smithells CJ, Gale WF, Totemeier TC. Smithells metals reference book. Boston: Elsevier Butterworth-Heinemann, 2004.

[22] Song M, Kovacevic R. P I Mech Eng B-J Eng 2003;217:73.

[23] Zhang W, Roy GG, Elmer JW, DebRoy T. J Appl Phys 2003;93:3022.

[24] Sheppard T, Wright DS. Met Technol 1979;6:215.

[25] Kozlowski PF, Thomas BG, Azzi JA, Hao W. Metall Trans A 1992;23:903.

[26] Kuester JL, Mize JH. Optimization techniques with Fortran. New York: McGraw-Hill, 1973.

[27] Perzyna P, Wojno W. Arch Mech 1966;18:85.

[28] Zhu XK, Chao YJ. J Mater Process Tech 2004;146:263.

[29] Deng Z, Lovell MR, Tagavi KA. J Manuf Sci E-T Asme 2001;123:647.

[30] Kong HS, Ashby MF. Mrs Bull 1991;16:41.

[31] Ren XJ, Yang QX, James RD, Wang L. J Mater Process Tech

[32] Schmidt H, Hattel J, Wert J. Model Simul Mater Sc 2004;12:143.

[33] Cho HH, Han HN, Hong ST, Park JH, Kwon YJ, Kim SH, Steel RJ. Mat Sci Eng a-Struct 2011;528:2889.

[34] Lebensohn RA, Tome CN. Acta Metall Mater 1993;41:2611.

[35] Beyerlein IJ, Lebensohn RA, Tome CN. Mat Sci Eng a-Struct 2003;345:122.

[36] Taylor GI. J I Met 1938;62:307.

[37] Asaro RJ, Needleman A. Acta Metallurgica 1985;33:923.

[38] Kim D, Badarinarayan H, Kim JH, Kim C, Okamoto K, Wagoner RH, Chung K. Eur J Mech a-Solid 2010;29:204.

[39] He X, DebRoy T, Fuerschbach PW. J Appl Phys 2004;96:4547.

[40] Halley PJ, Mackay ME. J Rheol 1994;38:41.

[41] Cho HH, Kang SH, Kim SH, Oh KH, Kim HJ, Chang WS, Han HN. Mater Design 2012;34:258.

[42] Lakshminarayanan AK, Balasubramanian V. Met Mater Int 2011;17:969.

Chapter 4

Microstructural analysis of friction stir welded steel with phase transformation

4.1 Introduction: Steel with phase transformation

Application of FSW to ferrous alloys including linepipe steel with high melting temperatures has been limited due to high temperatures and severe wear conditions induced by the welding tool during the process. However, continued research into this process has brought some success in the joining of ferrous alloys [1-3], and this practical success requires a clearer understanding of the FSW joints of ferrous alloys. Sato *et al.* [1] reported that FSW successfully produced the defect-free weld in ultrahigh carbon steel having the (ferrite + cementite) duplex structure using a polycrystalline cubic boron nitride (PCBN) tool, and FSW changed the (ferrite + cementite) duplex structure into the martensitic structure in the weld center. Cho *et al.* [3] also examined the microstructure and hardness of FSW joint of 409 ferritic stainless steel. They found that the increase in plunging depth increased the amounts of both heat input and plastic deformation to the welded material during FSW, which led to an increase in the fraction of low-angle boundary (LAB), a decrease in the grain size, and an increase in the hardness in the stir

zone (SZ). In particular, it is very important to understand the microstructural evolution of ferrous alloys during FSW because this understanding would enable a prediction of the weld properties resulting from the microstructures.

Sato *et al.* [4] examined the recrystallization phenomenon during friction stirring of 304L austenitic stainless steel by experimental approaches and found that friction stir processed 304L austenitic stainless steel underwent partial static recrystallization following dynamic recrystallization. Mironov *et al.* [5] examined the microstructural evolution of pure iron during friction stir-processing. They reported that the development of grain structure was driven mainly by grain subdivision, geometrical effect of strain and local grain-boundary migration.

The above-mentioned studies focused on face-centered cubic (FCC) and body-centered cubic (BCC) metals, in which a phase transformation does not occur during FSW. On the other hand, a solid-state phase transformation should be considered in the microstructural evolution of ferrous alloys including linepipe steel during FSW. This phenomenon is considered as a main factor affecting the properties of ferrous alloys, and studies concerning this phenomenon have been performed by many researchers [6-11]. Sato *et al.* [1] examined the microstructural evolution of ultrahigh carbon steel during FSW. However, this research focused mainly on the relationship between the microstructures and mechanical properties instead of the microstructural evolution of ultrahigh carbon steel. Furthermore, other studies in the field of

FSW for ferrous alloys focused mainly on the development of adequate tool materials due to the above-mentioned problems [12,13].

It should be noted that the development of grain structure of ferrous alloy is comprehensively investigated. Recently, linepipe steel has attracted noticeable attention in structural materials for its high strength, excellent low-temperature toughness and good weldability, and the application of FSW for this steel has been begun to use the advantages of a solid-state welding process. Therefore, in the field of FSW, studies of the microstructural evolution in high-strength linepipe steel (API grade X100) are greatly challenging. The present study focused on the fundamental issue of grain structure development during FSW of high-strength linepipe steel. For this purpose, an electron back-scatter diffraction (EBSD) equipped with field emission scanning electron microscope (FE-SEM) and a transmission electron microscope (TEM) were used to provide a comprehensive understanding of microstructural evolution during FSW of high-strength linepipe steel.

4.2 Experimental procedure

API X100 grade linepipe steel, 10 mm in thickness, was used in the FSW studies; Table 4.1 lists the chemical composition and carbon equivalent provided by a steel supplier, POSCO. The test plate was sectioned in half along the rolling direction and prepared for a butt joint. Oxide scale was removed by sand grinding followed by degreasing with methanol. An Ar atmosphere was maintained using a gas cup located around the tool to minimize surface oxidation during the weld cycle. Friction stir welding was performed with a PCBN tool (MegaStir Technologies, UT, USA) in an inert gas environment. The tool rotation and welding speeds were 450 rpm and 127 mm/min, respectively. The PCBN tool had a shoulder diameter of 16 mm and a pin diameter of 4 mm. The principal directions of FSW geometry are denoted as the welding direction (WD), transverse direction (TD) and normal direction (ND).

Following FSW, the plate was prepared perpendicular to the WD and examined by optical microscope (OM), EBSD equipped with FE-SEM and TEM. The surface for OM was prepared by mechanical polishing with a 1 μm diamond paste followed by chemical etching in 3 ml nitric acid + 97 ml methanol solution. For the EBSD observations, the sample was mechanically ground and electrolytically polished in a 10 ml perchloric acid + 90 ml ethanol solution using a Struers Lectropol-5 electrolytic polisher. For TEM

analysis, a thin slice was cut using a low-speed diamond saw and then mechanically thinned to nearly 100 μm thickness. Three millimeter discs were punched out and electro-polished in a Struers Tenupol-3 twin-jet polisher using using a solution containing 10% perchloric acid in methanol.

OM analysis was carried out using an Olympus GX51 optical microscope. High-resolution EBSD studies were performed using a Jeol JSM6500F FE-SEM equipped with a HKL Channel 5 EBSD system. The accelerating voltage was 20 kV, the probe current was 4 nA and the working distance was 15 mm with the sample stage tilted by 70°. The camera resolution was 978 x 733 pixels in the operation of 8 x 8 binning. The mapping grid was a regular square in 0.3 μm steps. The limits of the low-angle boundaries (LABs) and high-angle boundaries (HABs) were set to 2^{o} and 15^{o}, respectively. Based on this criterion, the grain sizes were measured using the linear intercept method. TEM analysis was carried out using a TECNAI F20 operating at a voltage of 200 keV.

The Vickers hardness test was conducted in a 4 x 11 array at 2 mm intervals on a cross section perpendicular to the WD using a commercial AIS 3000R (Frontics Inc., Seoul, Korea) with depth and load resolutions of 0.1 μm and 14.7 mN, respectively. The maximum depth, dwell time and testing speed were 70 μm, 0.5 sec and 5 μm/sec, respectively.

All microstructural analyses were made on a transversal (TD-ND) plane, which is identical to the cross-section perpendicular to the WD.

Table 4.1 Chemical composition and carbon equivalent (C_{eq}) of the examined API grade X100 linepipe steel.

Chemical composition (wt. %)								
C	Si	Mn	P	S	Nb	V	Mo	C_{eq}
0.05~0.07	0.25	≤2.0	≤0.01	≤0.001	≤0.05	≤0.05	≤0.3	0.46~0.48

4.3 Microstructural analysis: Steel with phase transformation

4.3.1 Base material

Figure 4.1 shows the microstructural features for the base material (BM). The microstructure consists mainly of the dual phases of ferrite and bainite with an average grain size of approximately 2.8 μm, as shown in Fig. 1a. The ferrite phase is almost equiaxed, whereas the bainite phase is subdivided into very fine laths. The misorientation-angle distribution is characterized by a sharp low-angle peak and some clustering of the misorientation axes near the <111> (Figure 4.1b) because the BM was produced by the rolling process. Therefore, the BM has a very weak rolling texture, as shown in Figure 4.1c.

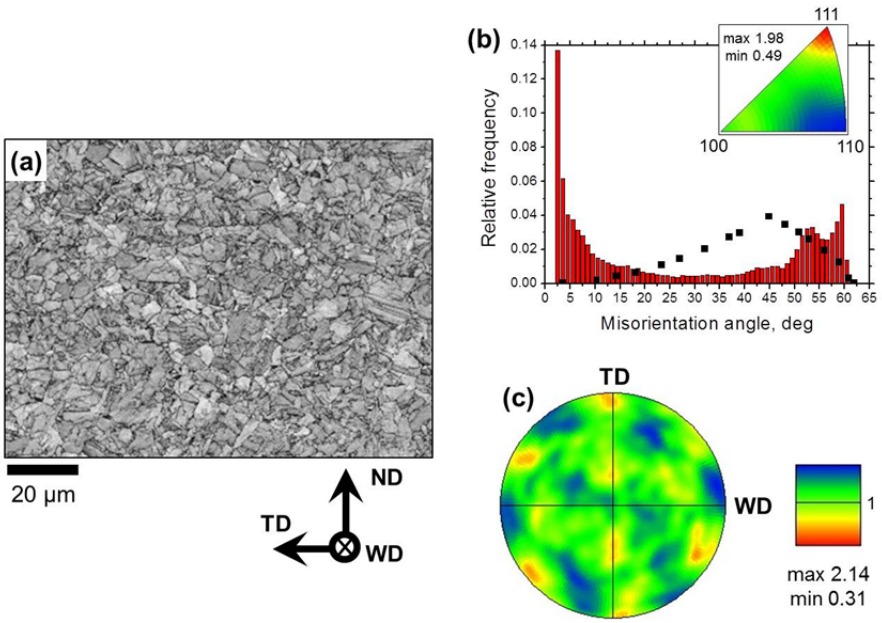

Figure 4.1 Characteristic microstructural features of the BM: (a) band contrast (BC) map showing the typical microstructure of API grade X100 linepipe steel; (b) misorientation-angle distribution (random distribution is shown by a dotted line); (c) {110} pole figure.

4.3.2 Low-magnification overview

Figure 4.2 shows a cross-sectional macrograph of the FSWed zone. In the cross section, the left- and right-hand sides of the weld center correspond to the retreating side (RS) and advancing side (AS) of the rotation tool, respectively. The FSW joint consists of a SZ, BM, broad transition region, which is commonly called the thermomechanically affected zone (TMAZ), and a heat affected zone (HAZ) between the TMAZ and the BM, even though it is difficult to clearly distinguish each zone. The SZ shows a basin-like shape that widens considerably towards the upper surface. The border region between the SZ and the BM is the TMAZ and HAZ.

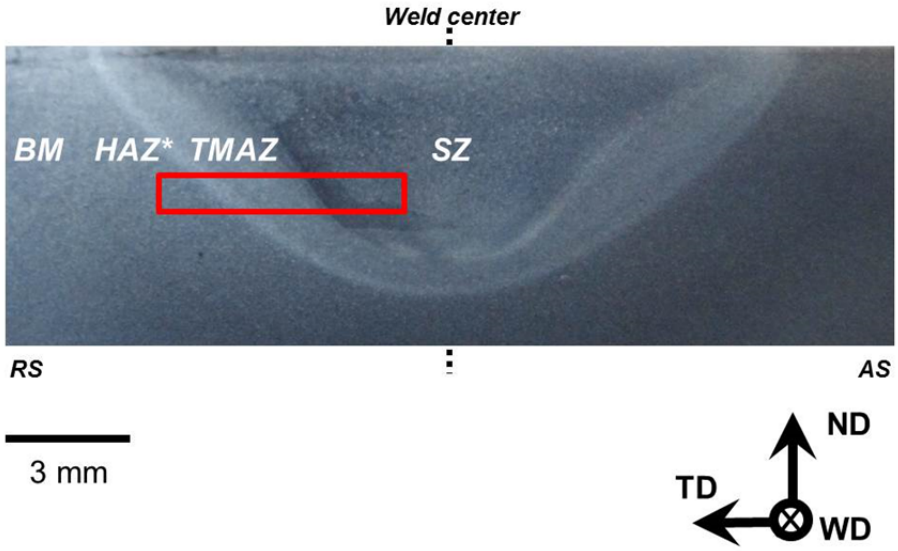

Figure 4.2 Cross-sectional macrograph of the welded sample. See text for details. RS and AS indicate the retreating and advancing sides, respectively.

4.3.3 Microstructural evolution

An examination how the original grain structure transforms to the SZ microstructure is needed to understand grain structure development during FSW [5,14,15]. Therefore, in the present study, the region marked by a red rectangle in Figure 4.2 was carefully analyzed. For the sake of simplicity, only microstructural evolution in the RS is described.

Figure 4.3 shows the EBSD maps taken from the region indicated by the red rectangle in Figure 4.2. Some selected areas (Regions 1, 2 and 3) in Figure 4.3 are shown at higher magnification in Figure 4.4a-c, respectively. In the EBSD maps in Figure 4.4a-c, the LABs and the HABs are depicted as white and black lines, respectively. The large EBSD map in Figure 4.3 is divided into three regions (HAZ, TMAZ and SZ) to quantify the microstructural evolution in the FSWed region, and the microstructural data measured from these regions is presented in Figure 4.5, 4.6, 4.7 and 4.8.

Figure 4.3 shows an orientation map including HAZ, TMAZ and SZ. The parent grains in the HAZ tend to grow due to the significant amount of heat generated during FSW. In the HAZ, the average grain size is about 3.3 μm, which is larger than that (2.8 μm) of the BM shown in Figure 4.1. On the center in the HAZ (Figure 4.4a), the original grains are homogeneously distributed, and the microstructure of this region is similar to that of the BM except for the grain size.

The crystallographic orientation of the parent grains does not change practically, as shown in Figure 4.5a. The fraction of LABs in the HAZ (Figure 4.6) is 39.6 %, which is slightly smaller than 43.8 % in the BM. This indicates that the removal or rearrangement of LABs occurred in the HAZ during the FSW process due to the increasing temperature of the material. Figure 4.7a shows the misorientation-angle distribution in the HAZ. The characteristic feature is a clustering of the misorientation axis near <110>. The LABs rearrange around <110> rotation axes by the significant heat generated during FSW, and consequently, a strong cluster in the misorientation-angle distribution develops.

In the TMAZ (Figure 4.3 and 4.4b), considerably fine homogeneous grains similar to those observed in the SZ of other steel alloys developed [1-5,15-17]. The fine-grained microstructure in the TMAZ was attributed to the continuous dynamic recrystallization induced by the substantial shear deformation and significant amount of heat generated during FSW. The average grain size is approximately 2.2 μm, which is the smallest value among the FSWed regions.

The continuous dynamic recrystallization, which is an interesting microstructural characteristic of the TMAZ, would be associated with the progressive transformation of sub-grains into new grains within the deformed grains as well described in the literature [18]. In other words, LABs accumulate progressively in the LABs within the deformed grains during

FSW, leading to an increase in their misorientation angle and the formation of HABs, when a critical value of the misorientation angle is reached. Then, migration of HABs eventually causes fine homogeneous grains in the TMAZ. This result is in agreement with the literature in which the continuous dynamic recrystallization well occurs in ferrite with a relatively larger stacking fault energy [19,20].

The shear texture weakly developed in the TMAZ, as shown in Figure 4.5b. The fraction of LABs in the TMAZ (Figure 4.6) is approximately 30 %, which is the smallest value among the FSWed regions. This is due to an increase in the HABs induced by the continuous dynamic recrystallization. The misorientation-angle distribution is featured by the increase in HABs in the overall range and the dispersed clustering of the misorientation axes near <110>, as shown in Figure 4.7b.

In the SZ (Figure 4.3 and 4.4c), the structure morphology, texture and misorientation-angle distribution are completely different from the other FSWed regions. The structure morphology observed in this region is quite distinguishing and can be elucidated adequately in terms of the phase transformation that occurs during FSW. Figure 4.9 shows the temperature-time profile measured at the tool shoulder during FSW. According to thermodynamic calculation using Thermo-Calc software [21], the A_1 and A_3 temperatures of the API grade X100 linepipe steel are 683 and 792 ^{o}C, respectively. During the experiment, the peak temperature measured at the

root of the tool shoulder is 983 ^{o}C (Figure 4.9), which is significantly higher than the A_1 and A_3 temperatures. Since the temperature of the material during FSW might be considerably higher than that of the root of the tool shoulder, it is likely that the temperature of the material in the SZ during FSW becomes higher than the A_1 and A_3 temperatures. Therefore, the austenite-to-ferrite transformation occurs in the SZ during FSW, and this phenomenon would result in a specific SZ completely different from the other FSWed regions.

Region 3 shows a typical SZ with acicular-shaped bainitic ferrites formed by a phase transformation during FSW (Figure 4.4c). In region 3, the original ferrite structure transforms fully to a single-phase austenite structure during the heating cycle of FSW. This steel then undergoes a solid-state transformation from austenite to acicular-shaped bainitic ferrite during the cooling cycle due to rapid cooling and a high strain induced by severe plastic deformation caused by frictional stirring [22,23]. The high-magnification inset in the bottom right corner of Figure 4.4c shows typical acicular-shaped bainitic ferrite with many LABs, and this is in accordance with the literature in which the dislocation density of bainitic ferrite in high-strength steel is quite high [24].

Figure 4.10a shows typical acicular-shaped bainitic ferrites in the SZ. As mentioned above, high density dislocations are distributed in these bainitic ferrites. In addition, shaves of acicular-shaped bainitic ferrites tend to grow as a series of parallel platelets emanating from the austenite grain boundary.

According to Borrato *et al.* [25], the recrystallization stop temperature (RST) in austenite, which is the minimum temperature that recrystallization can occur during hot rolling, is expressed as follows:

$$RST(^{o}C) = 887 + 464C + (6645Nb - 664\sqrt{Nb}) + (732V - 230\sqrt{V}) + 890Ti + 363Al - 357Si \quad (1)$$

where the chemical compositions are in weight percent.

The RST value of API grade X100 linepipe steel is 999 ^{o}C, which is slightly higher than the peak temperature (983 ^{o}C) measured at the root of the tool shoulder. Since the temperature of the material during FSW may be considerably higher than that of the root of the tool shoulder as mentioned above, it is likely that dynamic recrystallization occurs in the austenite phase in the SZ during FSW process. Therefore, very fine austenite grains would develop during FSW, which would lead to the formation of acicular-shaped bainitic ferrties that nucleate mainly at the austenite grain boundary. As a result, Figure 4.10a shows that the morphological characteristics of the SZ are completely different from those of the BM composed of ferrite and bainite, as shown in Figure 4.10b.

Figure 4.8 shows the profiles of the grain size and acicular-shaped phase fraction with an aspect ratio over 3 measured from the region indicated by the red rectangle in Figure 4.2. The criterion to classify the FSWed regions in the API grade X100 linepipe steel would not be the grain size but rather the acicular-shaped phase fraction. In the distribution of the acicular-shaped phase fraction, boundaries among the FSWed regions are quite distinct, whereas the boundary between the TMAZ and the SZ is ambiguous in that of the grain size. In other words, the acicular-shaped phase fraction decreases drastically at the boundary between the HAZ and the TMAZ due to the newly formed homogeneous grains in the TMAZ, and it considerably increases at that between the TMAZ and SZ because of the acicular-shaped bainitic ferrites developed by a phase transformation that occurs in the SZ.

The texture sharpens significantly close to <110> (achieving ~ 4.3 times random) as shown in Figure 4.5c. The fraction of LABs broadly increases as it approaches the center of the SZ (Figure 4.6) because typical acicular-shaped bainitic ferrites have many LABs as mentioned above. The misorientation-angle distribution is characterized by the increase in HABs in the angular range of 55~60^{o}. The newly developed acicular-shaped bainitic ferrites are typically surrounded by HABs, thus increasing the fraction of HABs.

Figure 4.11 summarizes the microstructural features for the RS in the SZ taken from the region indicated by the black dashed rectangle in Figure 4.8. The microstructural evolution in this region can be explained by its cooling

from the (ferrite+austenite) duplex structure. According to the reported calculation result [26], the peak temperature of the RS in the SZ is lower than that of the center in the SZ, which may allow the presence of a (ferrite+austenite) duplex structure below the A_3 temperature. Since the austenite phase transforms to bainitic ferrite during the cooling cycle, the microstructure of the RS in the SZ includes both acicular-shaped bainitic ferrite developed by a phase transformation and fine homogeneous ferrite induced by dynamic recrystallization, as shown in Figure 4.11a. The misorientation-angle distribution is distinctly different from the random distribution, but is similar to the center in the SZ (Figure 4.11b). Although the predominant deformation mode during FSW is expected to be simple shear [27-30], the texture of the RS in the SZ is broadly random, and this may be associated with a weakness of shear texture caused by a phase transformation, which occurs during FSW. The microstructural features of the AS in the SZ are very similar to those of the RS of the SZ, and are omitted in this paper.

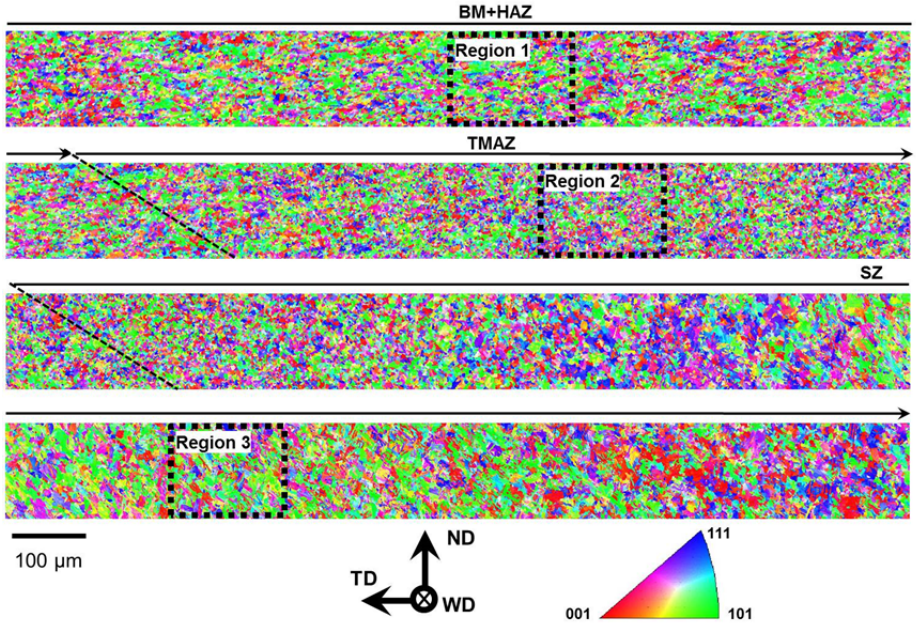

Figure 4.3 Composite EBSD map of HAZ, TMAZ and SZ on the RS of the weld. The individual grains are colored according to their crystallographic direction relative to the WD; the color code triangle is shown in the bottom right corner. See text for details.

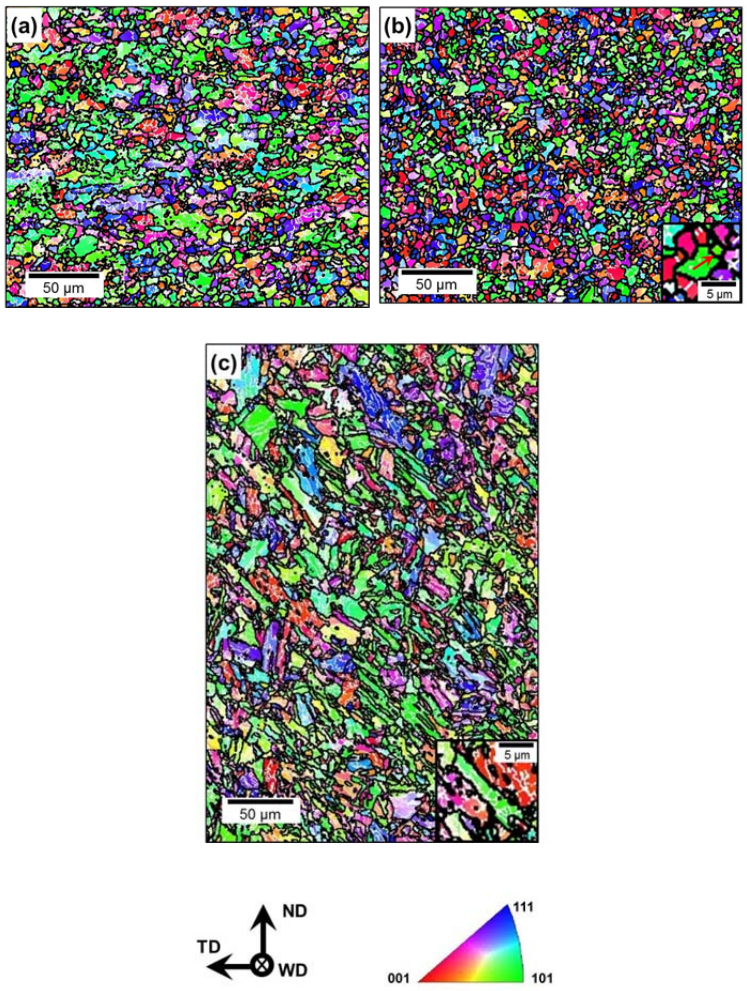

Figure 4.4 The orientation maps (a-c) of some selected areas (Regions 1, 2 and 3 in Figure 4.3). The individual grains are colored according to their crystallographic direction relative to the WD; the color code triangle is shown in the bottom center. LABs and HABs are depicted as white and black lines, respectively. See text for details.

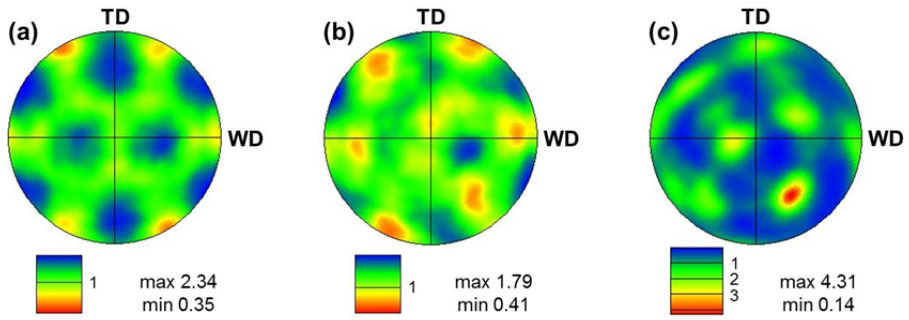

Figure 4.5 The {110} pole figures showing textures in (a) HAZ, (b) TMAZ and (c) SZ.

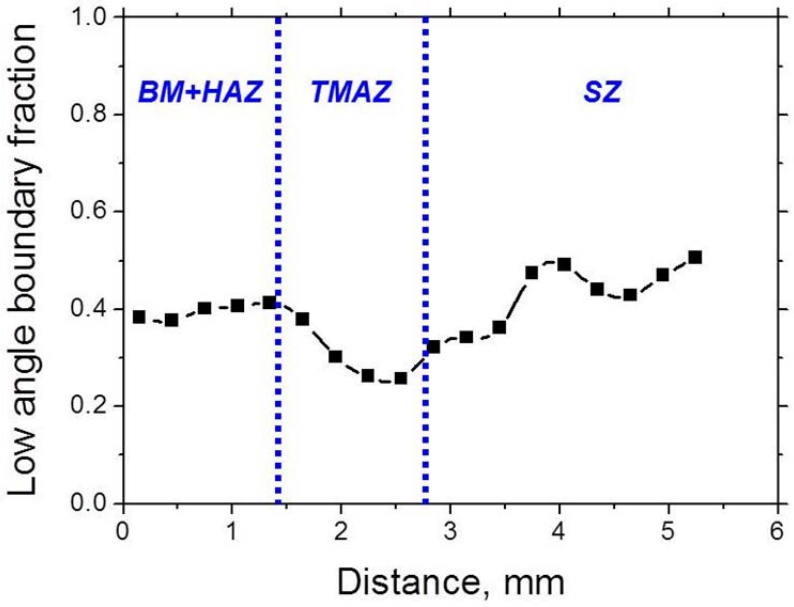

Figure 4.6 Profile of LABs fraction measured from the region indicated by the red rectangle in Figure 4.2.

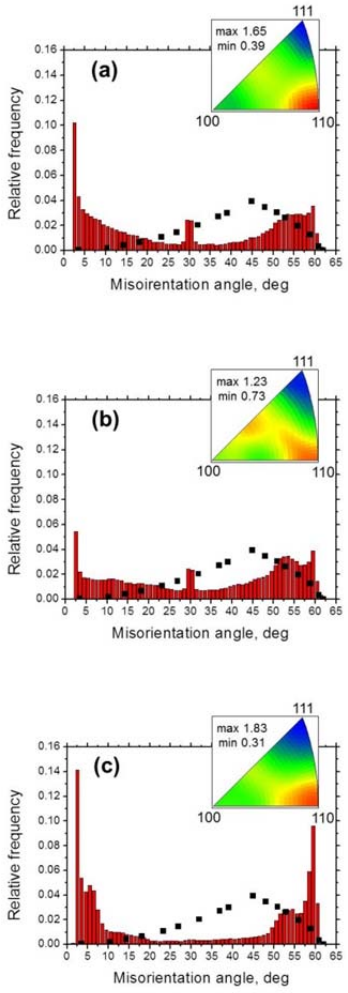

Figure 4.7 Misorientation-angle distributions in (a) HAZ, (b) TMAZ and (c) SZ. Misorientation-axis distributions are shown in the top right corners of the graphs, respectively.

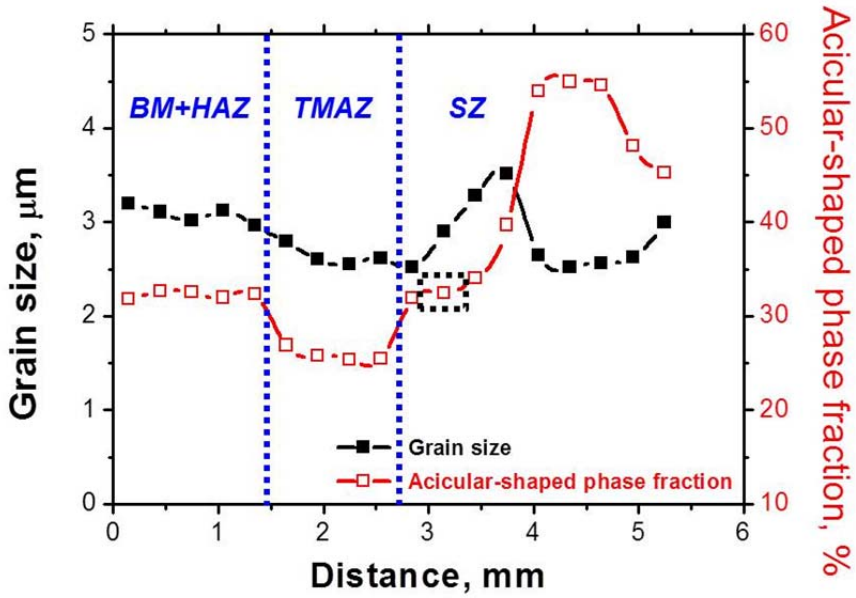

Figure 4.8 Profiles of grain size and acicular-shaped phase fraction with aspect ratio over 3 measured from the region indicated by the red rectangle in Figure 4.2.

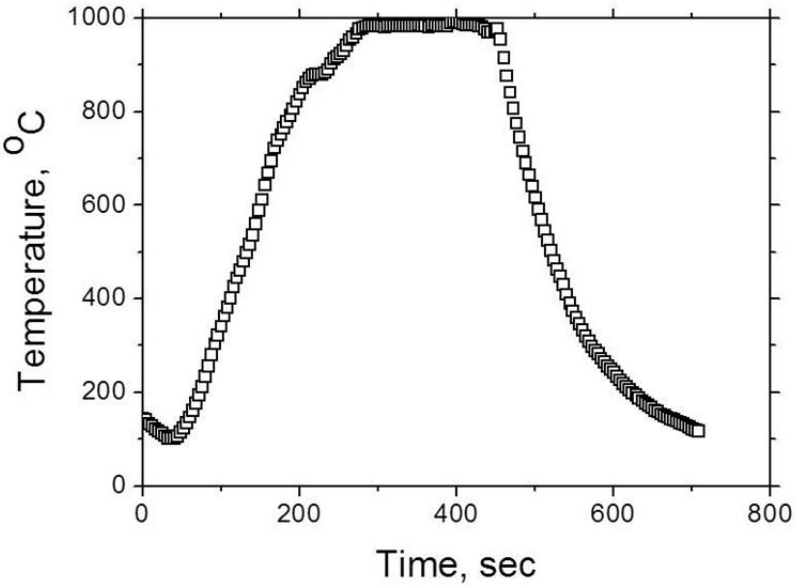

Figure 4.9 Temperature-time profile measured at the root of the tool shoulder.

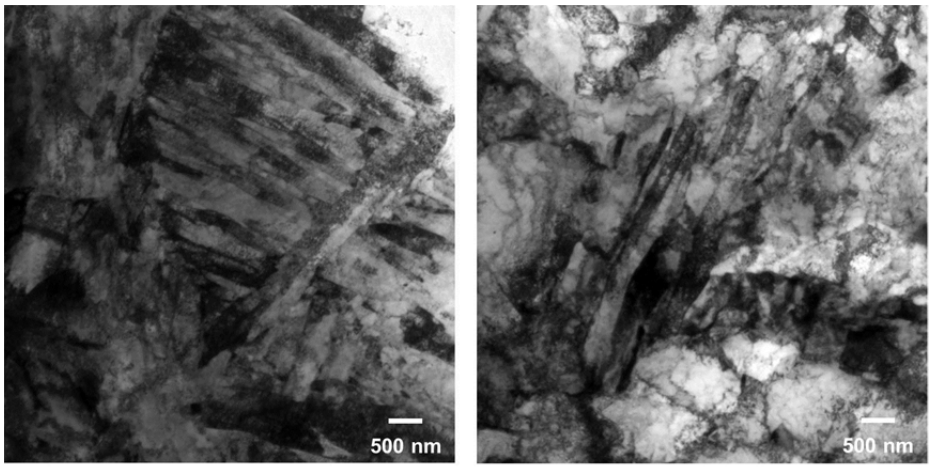

Figure 4.10 TEM micrographs showing the morphological characteristics of (a) SZ and (b) BM.

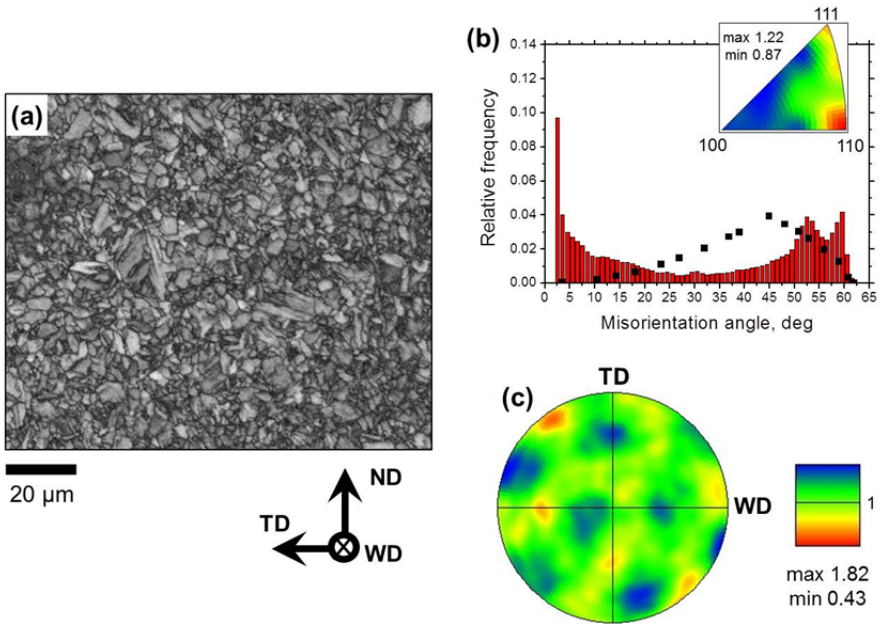

Figure 4.11 Characteristic microstructural features of the RS of the SZ: (a) band contrast (BC) map; (b) misorientation-angle distribution (random distribution is shown by a dotted line); (c) {110} pole figure.

4.3.4 Hardness distribution

Figure 4.12 shows a cross-sectional macrograph of the FSWed region with indentation marks. Figure 4.13 presents the corresponding hardness profile variations on the transversal lines (a-d) of indentation marks shown in Figure 4.12. From these figures, it can be verified that the hardness of the SZ is significantly higher than that of the other FSWed regions. This may be due to the development of bainitic ferrite caused by a phase transformation that occurs in the SZ during FSW [31]. On the other hand, the hardness of the HAZ is lowest among the FSWed regions because the grains in the HAZ tend to grow due to the significant heat generated during FSW.

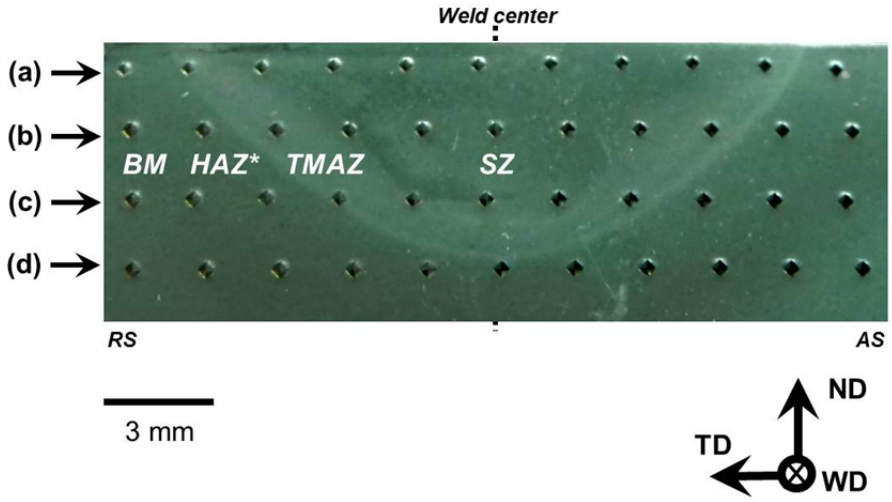

Figure 4.12 Cross-sectional macrograph of the welded sample with indentation marks.

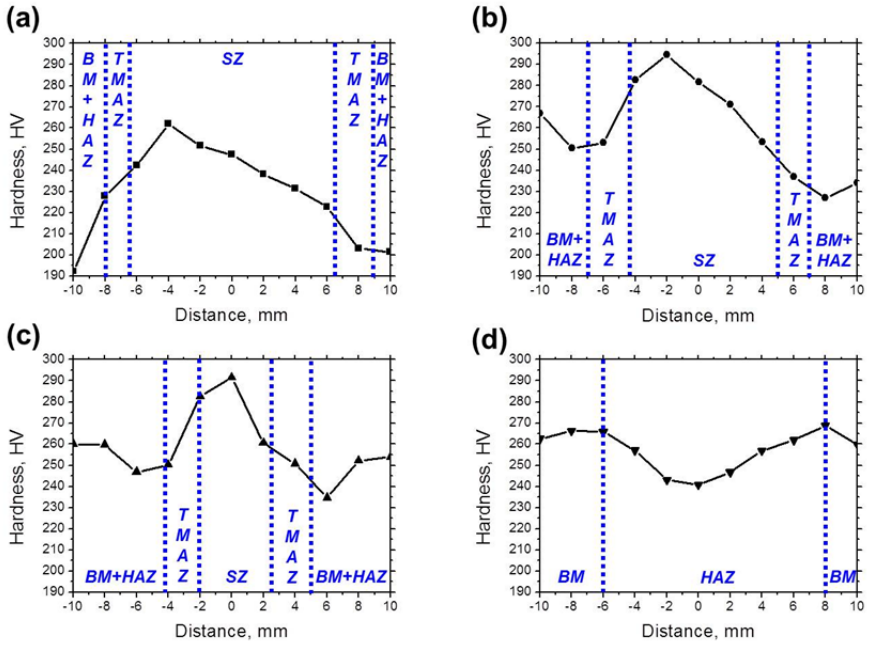

Figure 4.13 Profiles of hardness on each line (a-d in Figure 4.12) for welded sample.

4.4 Conclusion: Steel with phase transformation

The microstructural evolution of API X100 grade linepipe steel during FSW was examined using EBSD equipped with FE-SEM, OM and TEM. Grain structure evolution was found to be a complex process involving the rearrangement of LABs, continuous dynamic recrystallization and phase transformation. In the HAZ, the LABs rearrange around the <110> rotation axes by the significant heat generated during FSW. Fine homogeneous grains were mainly developed in the TMAZ, where continuous dynamic recrystallization occurs. Acicular-shaped bainitic ferrites were observed in most parts of the SZ, and the fraction of these could be a quite distinct criterion to distinguish the FSWed regions. Although FSW causes shear texture in the SZ as known, the texture in the SZ was quite random due to the weakness of shear texture induced by a phase transformation that occurs in the SZ during FSW. The hardness of the SZ is significantly higher than that of the other FSWed regions because of the bainitic ferrites that developed as a result of a phase transformation during FSW.

4.5 References

[1] Sato YS, Yamanoi H, Kokawa H, Furuhara T. Scripta Mater 2007;57:557.

[2] Bhadeshia HKDH, Debroy T. Sci Technol Weld Joi 2009;14:193.

[3] Cho HH, Han HN, Hong ST, Park JH, Kwon YJ, Kim SH, Steel RJ. Mater Sci Eng A 2011;528:2889.

[4] Sato YS, Nelson TW, Sterling CJ. Acta Mater 2005;53:637.

[5] Mironov S, Sato YS, Kokawa H. Acta Mater 2008;56:2602.

[6] Han HN, Lee JK. ISIJ Int 2002;42:200.

[7] Han HN, Lee CG, Oh CS, Lee TH, Kim SJ. Acta Mater 2004;52:5203.

[8] Han HN, Lee JK, Suh DW, Kim SJ. Philos Mag 2007;87:159.

[9] Han HN, Lee CG, Suh DW, Kim SJ. Mater Sci Eng A 2008;485:224.

[10] Han HN, Oh CS, Kim G, Kwon O. Mater Sci Eng A 2009;499:462.

[11] Lee MG, Kim SJ, Han HN. Int J Plasticity 2010;26:688.

[12] Mahoney M, Nelson TW, Sorenson C, Packer S. Mater Sci Forum 2010;638:41.

[13] Mishra RS, Mahoney MW. Friction Stir Welding and Processing. first ed.. USA: ASM International, 2007.

[14] Mironov S, Sato YS, Kokawa H. Acta Mater 2009;57:4519.

[15] Suhuddin UFHR, Mironov S, Sato YS, Kokawa H, Lee CW. Acta Mater 2009;57:5406.

[16] Reynolds AP, Tang W, Gnaupel-Herold T, Prask H. Scripta Mater 2003;48:1289.

[17] Sato YS, Nelson TW, Sterling CJ, Steel RJ, Pettersson CO. Mater Sci Eng A 2005;397:376.

[18] Gourdet S, Montheillet F. Acta Mater 2003;51:2685.

[19] Schramm RE, Reed RP. Metall Mater Trans A 1975;6A:1345.

[20] Vecchio KS, Hertzberg RW. J Mater Sci 1988;23:2220.

[21] Thermo-Calc, Version S, Foundation of Computational Thermodynamics, Royal Institute of Technology, Stockholm, Sweden, 2008.

[22] Strangwood M, Bhadeshia HKDH. Advances in Welding Technology and Science 1987;1:209.

[23] Yang JR, Bhadeshia HKDH. Advances in Welding Technology and Science 1987;1:187.

[24] Farrar RA, Harrison PL. J Mater Sci 1987; 22:3812.

[25] Borrato F, Barbosa R, Yue S, Jonas JJ. Thermec-88 1988;1:383.

[26] Cho JH, Kang SH, Han HN, Oh KH. Met Mater Int 2008;14:247.

[27] Prangnell PB, Heason CP. Acta Mater 2005;53:3179.

[28] Fonda RW, Bingert JF, Colligan KJ. Scripta Mater 2004;51:243.

[29] Reynolds AP, Hood E, Tang W. Scripta Mater 2005;52:491.

[30] Park SHC, Sato YS, Kokawa H. Metall Mater Trans A 2003;34A:987.

[31] Sung HK, Shin SY, Hwang BC, Lee CG, Kim NJ, Lee SH. Kor J Met Mater 2010;48:798.

Chapter 5

Numerical investigation on friction stir welding of steel with phase transformation

5.1 Introduction: Phase transformation behavior in FSW

A solid-state phase transformation should be considered in the numerical model if it occurs during FSW. This phenomenon is considered as a main factor affecting the properties of the steel, and studies concerning this phenomenon have been performed by many researchers. Especially, during FSW, significant heat and severe plastic deformation would affect mainly austenite grain size (AGS) which is one of main factors to determine the phase transformation behavior of the steel. Thus, we should determine AGS during FSW to incorporate precise phase transformation behavior into the numerical model.

Austenite grain size evolution models have been proposed by many researchers [1-15]. Sellars *et al.* developed microstructural evolution models as a function of strain, strain rate, temperature, and initial grain size [1-3]. Most of applications of these studies were concentrated on hot rolling processes [3-6]. After that, many AGS evolution models have benn developed [7-15], and these models were incorporated into the numerical model.

In this study, we present the thermo-mehcanical model coupled with the phase transformation model. First, appropriate AGS evolution model is incorporated into the phse transformation model to predict precise phase transformation behavior during FSW. The phase transformation model is coupled with the numerical model in previous section. The computed results agree well with the measured temperature distribution and phase fraction.

5.2 Numerical modeling

5.2.1 AGS evolution model

AGS evolution model describes the change of AGS by recrystallization and grain growth. Generally, AGS evolution models are divided into dynamic, static, and meta-dynamic recrystallization processes. If the strain value is more than the critical strain, dynamic recrystallization (DRX) occurs. The critical strain for DRX is calculated as follows:

$$\varepsilon_c = 3.92 \times 10^{-4} d_o^{0.5} (\dot{\varepsilon} \exp(312000/RT))^{0.15} \quad (1)$$

where ε_c, d_o, and $\dot{\varepsilon}$ are the crital stain for DRX, the initial AGS, and the strain rate, respectively. The order of crital strain is one order of magnitude. Since strain develops during FSW is about two orders of magnitude, DRX would occurs in austenite region during FSW. Thus, AGS evolution model during FSW could be described as follows:

$$AGS = 1.5 \times 10^{3} (\dot{\varepsilon} \exp(Q/RT))^{-0.23} \quad (2)$$

where Q is the activation energy, and its value is 240 KJ/mol in C-Mn steel [12]. AGS is a function of strain rate and temperature, and this equation could

be applied to the phase transformation model. Figure 5.1 shows the variation of AGS with strain rate and temperature. AGS decreases with increasing strain rate and decreasing temperature. When the strain rate is higher than the critical value, AGS is saturated due to the equilibrium between hardening and energy releasing rates.

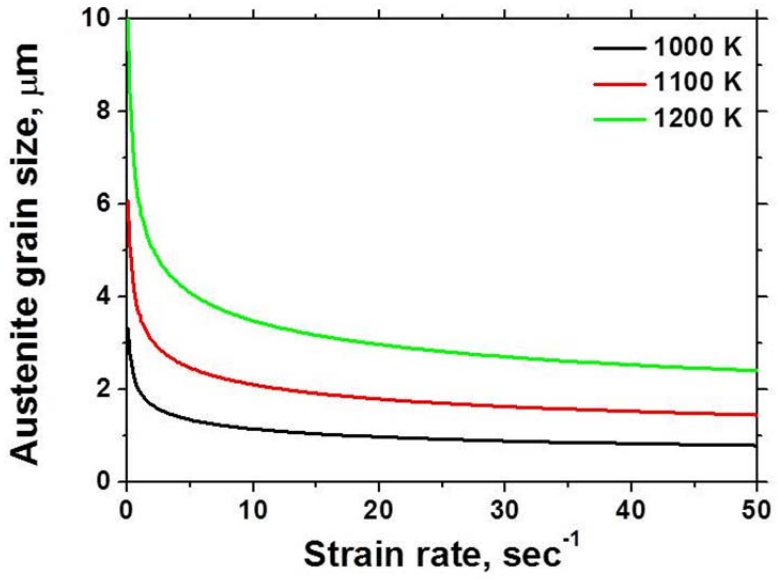

Figure 5.1 Profiles of AGS with strain rate and temperature.

5.2.2 Incorporating phase transformation model into the thermo-mechanical model

The transformation kinetics of the decomposition of austenite could be characterized using a Johnson-Mehl-Avrami-Kolmorgorov (JMAK) type equation as follows:

$$X = 1 - \exp(-kt^n) \tag{3}$$

where X is the transformed phase fraction, and t is the total time for the transformation at a given temperature. n is the time exponent and k is the parameter, depending on the temperature, composition, thermodynamic data, and AGS. The AGS evolution model was incorporated into the k value, and consequently, the phase transformation model was coupled with the thermo-mehcanical model.

5.3 Thermo-mechanical behavior of steel with phase transformation

The FSW process is simulated with the thermo-mechanical model and phase transformation model presented in the previous section. The computed temperature profile along the longitudinal section around the tool is shown in Figure 5.2. The temperature profile on the longitudinal midsection is compressed in the front of the tool and expanded behind the tool. The computed peak temperature is 1190 K. The computed results demonstrate that phase transformation occurs during FSW process of mild steel (SPCC) since Ae_1 (982 K) and Ae_3 (1123 K) temperatures are smaller than the peak temperature.

Figure 5.3 shows the computed thermal histories around the tool. The result shows that temperature increases rapidly during heating and decreases slowly during cooling. Figure 5.4 shows temperature distribution measured during FSW process using thermo-graphic camera. The measured peak temperaute is 1193 K at emissivity of 0.465. The computed results matched reasonably well with the experimental data, and this good agreement indicates that the model can be used to predict temperature profiles and histories during FSW.

Figure 5.5 shows the computed phase fraction distributions of ferrite and bainite during FSW. The results demonstrate that the ferrite phase is

developed during FSW, and bainite transformation follows ferrite transformation as shown in Figure 5.5. Figure 5.6 shows the computed phase fraction histories during FSW. Initially, ferrite phase is decomposed of austenite phase, and then austenite phase is transformed into ferrite and bainite phases. These computed results show that the SZ consists of mainly ferrite phases. Figure 5.7 shows (i) orientation maps, (ii) misorienation-angle distributions, and (iii) {110} pole figures of the BM and the center region of the SZ, respectively. Ferrite phases develop in the two regions, and there is little difference in microstructural characteristics between two regions. Figure 5.8 shows the computed heat of transformation during FSW. The result indicates that transformation induced heat occurs mainly in the SZ. The heat would affect peak temperature of the material during FSW.

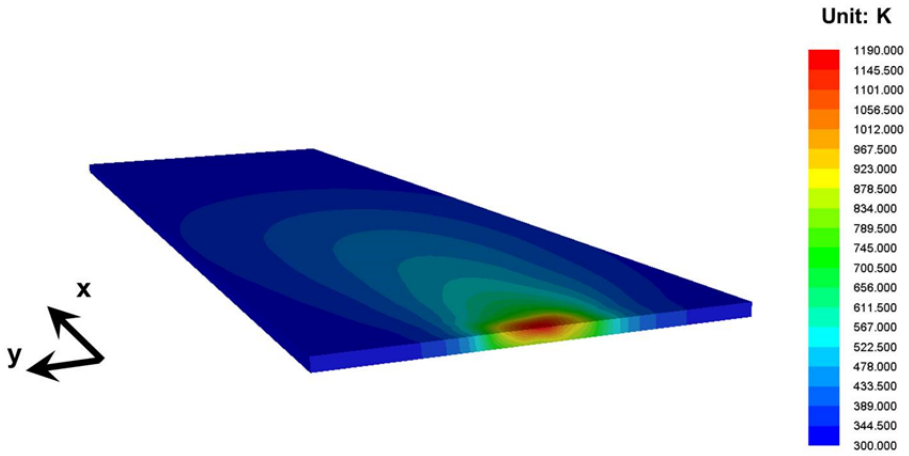

Figure 5.2 Computed temperature profile in x = 2.85 mm (yz-plane, xy-plane) for the welding condition of 1600 rpm and 3.3 mm/sec.

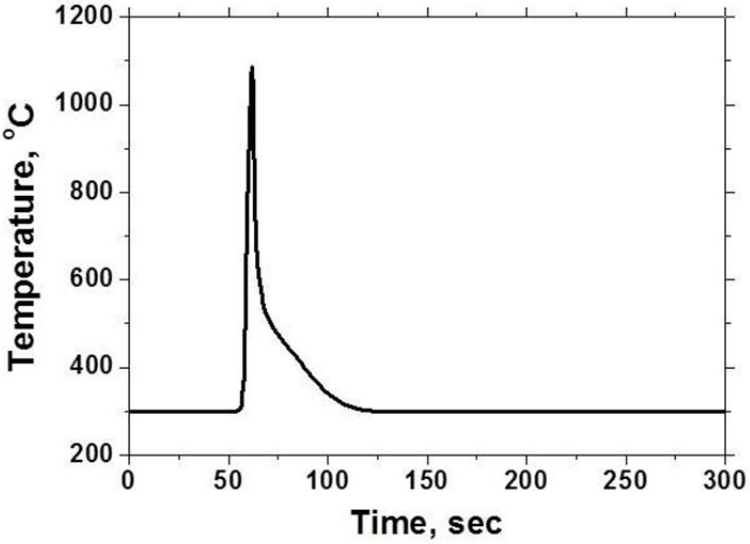

Figure 5.3 Computed time-temperature profile around the tool.

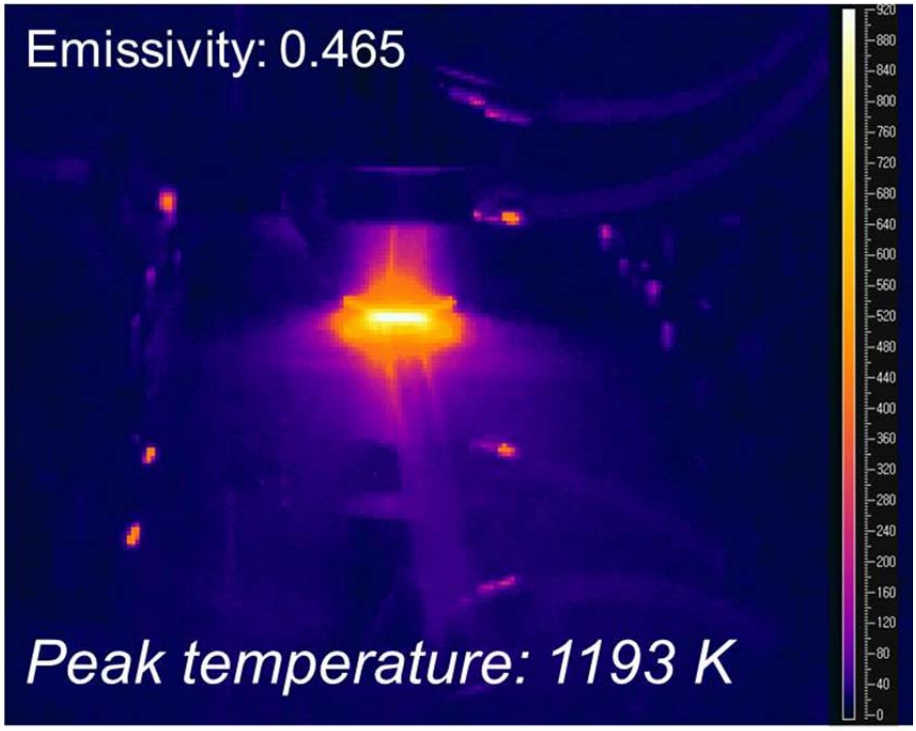

Figure 5.4 Temperature distribution measured during FSW process using thermo-graphic camera.

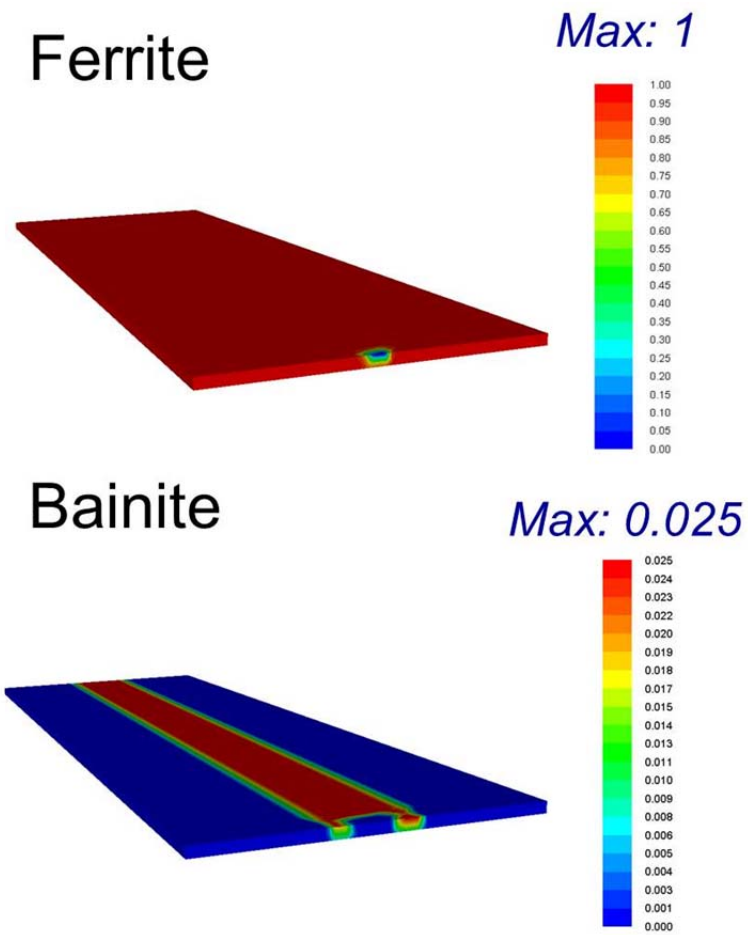

Figure 5.5 Computed phase fraction distributions of ferrite and bainite during FSW.

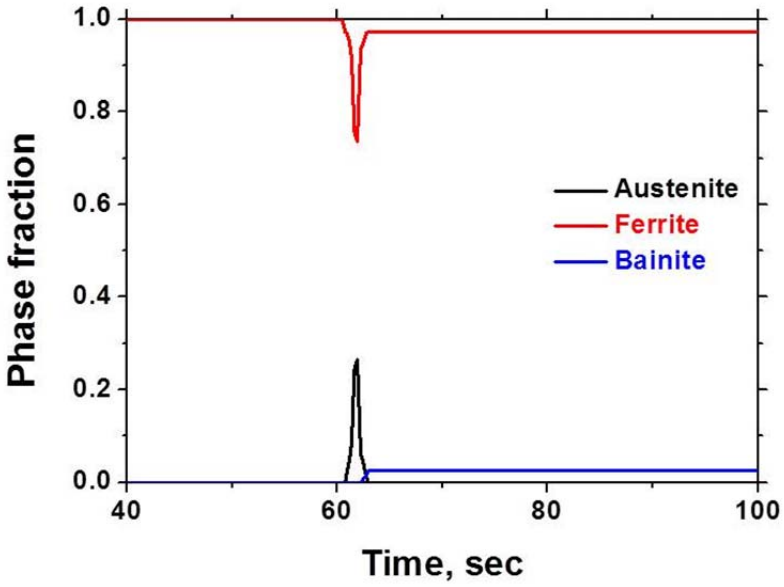

Figure 5.6 Computed phase fraction histories during FSW.

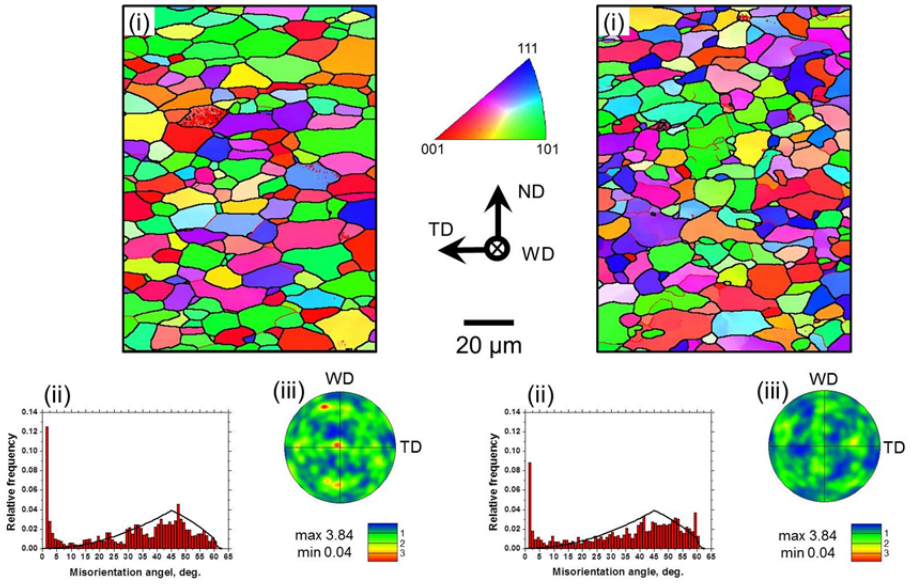

(a) (b)

Figure 5.7 (i) Orientation map, (ii) misorientation-angle distribution (random distribution is shown by a solid line) and (iii) {110} pole figure of (a) BM and (b) FSWed region, respectively. WD, TD and ND correspond to welding, transversal and normal directions, respectively.

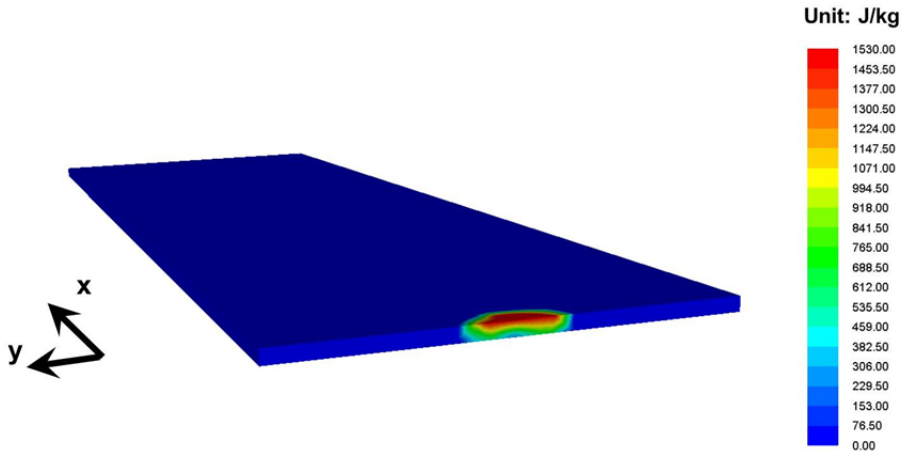

Figure 5.8 Computed heat of transformation profile in x = 2.85 mm (yz-plane, xy-plane).

5.4 Conclusion

The developed thermo-mechanical model was coupled with the phase transformation model. Frictional heat and severe plastic deformation affects phase transformation behavior of SPCC steel during FSW. Especially, AGS changes significantly during FSW, and the appropriate AGS model was coupled with the phase transformation model. The measured temperature distribution and phase fraction agreed fairly well with the predicted data. Transformation induced heat occurs mainly in the SZ during FSW.

5.5 References

[1] Sellars CM, Whitemann JA. Met Sci 1979;13:187.

[2] Beynon JH, Sellars CM. ISIJ Int 1992;32:359.

[3] Sellars CM. Mater Sci Technol 1985;1:325.

[4] Suehiro M, Sato K, Tsukano Y, Yada H, Senuma T, Matsumura Y. Trans Iron Steel Inst Jpn 1987;27:439.

[5] Saito Y, Shiga C. ISIJ Int 1992;32:414.

[6] Kwon O. ISIJ Int 1992;32:350.

[7] Lee DL, Yue S, Choo WY. J Korean Inst Met Mater 2001;39:655.

[8] Maccagno TM, Jonas JJ, Hodgson PD. ISIJ Int 1996;36:720.

[9] Lee Y, Choi S, Hodgson PD. Mater Sci Eng A 2002;336:177.

[10] Kwon HC, Lee Y, Kim SY, Woo JS, Im YT. ISIJ Int 2003;43:676.

[11] Kwon HC, Lee Y, Im YT. ISIJ Int 2003;43:1967

[12] Hodgson PD, Gibbs RK. ISIJ Int 1992;32:1329.

[13] Karhausen K, Kopp R. Steel Res 1992;63:247.

[14] Yanagimoto J, Liu J. ISIJ Int 1999;39:171.

[15] Yanagimoto J, Ito T, Liu J. ISIJ Int 2000;40:65.

Chapter 6

Total conclusions

Friction stir welding (FSW) is a solid state joining process invented by The Welding Institute (TWI, UK) in 1991. The process leads to lower residual stress and distortion in comparison with the fusion-based welding processes, since no melting of the material occurs during the process. Also, the process reduces manufacturing costs on account of the elimination of defects, shielding gas, and costly weld preparation. In addition, the process produces high-quality joints with a finer homogeneous microstructure and superior mechanical properties compared with the fusion-based welding processes.

Initially, the FSW process was used only for non-ferrous alloys with a low melting temperature, such as aluminum alloys. In contrast, application of FSW to ferrous alloys including high strength steel with high melting temperatures has been limited due to high temperatures and severe wear conditions induced by the welding tool during the process. However, continued research into this process has brought some success in the joining of ferrous alloys, and this practical success requires a clearer understanding of the FSW joints of ferrous alloys. In this thesis, the thermo/mechanical behavior in FSW of steel was investigated based on the microstructural and numerical approaches. Also, the simulated results were directly compared

with the experimental results for validation of the developed model.

Firstly, the microstructural change in the FSWed region of steel, where phase transformation does not occur, was analyzed. High-quality, defect-free welds were successfully produced in the ferritic SS by FSW using a PCBN tool at a tool rotation speed of 600 rpm and a welding speed of 254 mm/min. A remarkably fine-grained microstructure was obtained in the SZ by dynamic recrystallization due to severe shear deformation and high heat generated during FSW process. The resulting smaller grains increased the hardness of the SZ. The fraction of LAB in the SZ was significantly increased as compared to that in the BM, and the texture in the SZ was very close to a shear texture in bcc materials. Lastly, the increase in plunging depth increased the amounts of both heat input and plastic deformation to the welded material during FSW, which led to an increase in the fraction of LAB, a decrease in the grain size, and an increase in the hardness in the SZ.

Secondly, three-dimensional heat transfer and material flow during the FSW of 409 ferritic stainless steel have been computed by solving the governing equations of mass, momentum, and energy using temperature-dependent physical properties. The non-Newtonian viscosity was determined from the computed values of strain rate, temperature and material properties. The computed results show that temperature increases rapidly around the tool mainly due to the heat generated at the interface between the tool and the workpiece. The computed results also show typical asymmetric temperature

distribution along the welding and transverse directions due to the rotational and linear motion of the tool. This asymmetric behavior becomes more prominent as the welding speed increases. The computed effective strain rate increases rapidly around the tool, where severe shear deformation occurs by intense friction stirring. In contrast, the computed viscosity decreases rapidly around the tool, where the flux of the material occurs. The computed temperature histories agreed well with the experimental results, and the morphology of the computed viscosity contour was identical to that of the real FSWed region. The computed streamlines indicate that the streamlines around the tool are nearly circular, closed forms. Also, the computed streamlines illustrate that the material flow occurs mainly on the RS of the tool. The texture around the FSW tool was predicted from the computed velocity gradients along the streamlines of the flow field. The shear deformation texture was significantly developed around the tool, and the computed texture agreed fairly well with the experimental data. A remarkably fine-grained microstructure was obtained in the SZ by continuous dynamic recrystallization due to the severe shear deformation and high heat generated during the FSW process. The fraction of LAB in the SZ was significantly increased compared to that in the base material. Finally, it was confirmed that the changes of the microstructural characteristics during/after the FSW process are closely related to those of the temperature, strain rate, viscosity, material flow and texture computed using the numerical model.

Thirdly, the microstructural evolution of API X100 grade linepipe steel with phase transformation during FSW was examined using EBSD equipped with FE-SEM, OM and TEM. Grain structure evolution was found to be a complex process involving the rearrangement of LABs, continuous dynamic recrystallization and phase transformation. In the HAZ, the LABs rearrange around the <110> rotation axes by the significant heat generated during FSW. Fine homogeneous grains were mainly developed in the TMAZ, where continuous dynamic recrystallization occurs. Acicular-shaped bainitic ferrites were observed in most parts of the SZ, and the fraction of these could be a quite distinct criterion to distinguish the FSWed regions. Although FSW causes shear texture in the SZ as known, the texture in the SZ was quite random due to the weakness of shear texture induced by a phase transformation that occurs in the SZ during FSW. The hardness of the SZ is significantly higher than that of the other FSWed regions because of the bainitic ferrites that developed as a result of a phase transformation during FSW.

Lastly, the developed thermo-mechanical model was coupled with the phase transformation model. Frictional heat and severe plastic deformation affects phase transformation behavior of SPCC steel during FSW. Especially, AGS changes significantly during FSW, and the appropriate AGS model was coupled with the phase transformation model. The measured temperature distribution and phase fraction agreed fairly well with the predicted data.

Transformation induced heat occurs mainly in the SZ during FSW.

From this study, thermo/mechanical behavior in FSW of steel, which has not been clear up to now, was described well. The developed model and suggested method lead to a clearer understanding about FSW of ferrous alloys. Furthermore, the rigorous numerical model coupled with experimental results demonstrated sufficient possibilities, which can predict directly the changes of microstructural characteristics during the FSW process.

국문 초록

마찰교반용접(FSW)은 고상에서 재료를 접합할 수 있는 매우 획기적인 기술로서, 1991년 영국의 TWI(The Welding Institute)에서 처음으로 개발되었다. 이 용접 방법은 액상에서 고상으로 가는 과정이 공정 중에 일어나지 않기 때문에 일반적인 용접 방법에 비해 잔류 응력과 뒤틀림, 결함 등을 최소화할 수 있다. 또한, 이 공정은 보통 접합부에 미세한 결정립을 발달시킴으로써 기계적 강도를 향상시키는 장점을 가지고 있기 때문에 다른 일반적인 용접 방법의 대안으로 떠오르고 있다.

마찰교반용접은 초기에는 녹는점이 낮은 재료, 즉 알루미늄 합금 같은 재료에 주로 적용되어 왔다. 반면에, 강도가 높은 재료, 즉 철강 같은 녹는점이 높은 재료에는 그 적용이 제한되어 있는 실정이었다. 그러나, 툴의 발달과 공정의 최적화에 관한 연구가 차츰 축적됨으로써, 강도가 높은 철강 계열에도 최근에는 이 공정이 적용되고 있다. 본 고에서는 실험과 전산모사 방법을 결합함으로써 철강의 마찰교반용접에서의 열적/기계적 거동을 기술하였다. 이에 더하여 계산된 결과들은 실험 결과들을 직접적으로 예측하기 위해 비교되었고, 검증되었다.

먼저, 마찰교반용접 중에 상변태가 일어나지 않는 강의 미세조직 변화가 분석되었다. 409 페리틱 스테인리스 강을 마찰교반용접을 통해 성공적으로 접합시켰으며, 우수한 강도의 접합부를 도출하였다. 현저하게 미세한 결정립이 접합부에서 관찰되었으며, 이는 연속동적 재결정에 의한 현상이라 판단되었다. 또한, 소각 입계가 접합부에서 기본 재료에 비해 상당히 증가하였다. 툴 삽입 깊이가 증가함에 따라 소각 입계와 경도가 증가하였고, 반면에 결정립 크기는 감소하였다.

다음으로, 마찰교반용접에 대한 열-기계적 모델을 Eulerian 유한체적법을 이용하여 개발하였으며, 정상상태하에서 FSW 공정 중의 열적/기계적 거동 변화를 예측하였다. 계산된 결과들은 측정된 온도 변화 이력과 미세조직 변화와 비교되었고, 검증되었다. 점소성 self-consistent 접근법을 이용하여 접합부의 집합조직이 예측되었고, 툴 근처에서 재료의 유동이 계산되었다. 계산된 결과를 통해, 열은 주로 재료와 툴의 경계에서 발생하는 것을 확인하였고, 점성도는 교반부와 열-기계적 영향부에서 급격하게 변화하는 것을 확인하였다. 재료의 유동은 주로 툴의 회전방향과 진행방향이 반대인 지점에서 발생하는 것을 예측하였다. 또한, 계산을 통해 접합부에서는 주로 전단 집합조직이 발달하는 것을 확인하였다.

측정된 온도 변화 이력과 미세조직적 특성은 계산된 결과와 잘 일치하였다.

다음으로, 상변태가 공정 중에 일어나는 강의 미세조직 변화가 분석되었다. 다양한 미세조직이 접합부 지역에서 발달하게 되는데, 발달된 미세조직들은 소각 입계의 재배열, 연속동적 재결정, 상변태에 의해 설명될 수 있다. 교반부의 대부분에서는 바늘모양의 베이나이틱 페라이트가 상변태에 의해 생성되었다. 연속동적 재결정이 일어나는 열-기계적 영향부에서는 미세한 결정립이 분포되어 있는 미세조직을 관찰할 수 있었다. 또한, 교반부에서는 상변태로 인해 전단 집합조직이 관찰되지 않았으며, 교반부의 경도는 상변태로 인해 발달된 상으로 인해 다른 접합부보다 높게 관찰되었다.

마지막으로, 개발된 열-기계적 모델에 상변태 모델을 결합하여 공정 중에 강의 상변태가 어떻게 진행되는지를 예측하였다. 마찰열과 과도한 소성 변형은 공정 중에 있는 강의 상변태에 큰 영향을 미친다. 따라서 열간 압연 중에서 흔히 사용되는 오스테나이트 결정립 크기 모델을 적용함으로써 적당한 상변태 모델을 만들고 이를 기존의 열-기계적 모델에 결합하였다. 측정된 온도와 상분율이 계산된 결과와 잘 일치하였다.

본 연구를 통해, 아직까지 명확하지 밝혀지지 않았던 철강의 마찰교반용접 중의 열적/기계적 거동을 분명하게 이해할 수 있었다. 개발된 모델과 제안된 방법은 철강의 마찰교반용접의 열적/기계적 거동에 대한 근본적인 이해를 가능하게 하였으며, 더욱이 개발된 모델은 계산만으로도 마찰교반용접으로 인해 나타나는 미세조직적 특징 변화들을 직접적으로 예측할 수 있는 충분한 가능성을 증명해 주었다.

핵심어: 마찰교반용접, 교반부, 열-기계적 영향부, 열 영향부, 페리틱 스테인리스 강, 고강도강, 연속동적 재결정, 동적 회복, 삽입 깊이, 열-기계적 모델, Eulerian 유한체적법, 점소성 self-consistent 접근법, 전단 집합조직, 재료 유동, 점성도, 소성 변형, 상변태, 바늘모양의 베이나이틱 페라이트, 경도, 오스테나이트 결정립 사이즈 모델

Student number: 2008-20689

감사의 글

I would like to dedicate this thesis to my loving parents and wife. (자식을 위해 평생 헌신하신 부모님과 사랑하는 아내에게 이 논문을 바칩니다.)

Brief Curriculum Vitae

Hoon-Hwe Cho

(C.P.) +82-10-6654-2624
(E-mail) ccekkan7@snu.ac.kr

Education

Mar. 2008 ~ present : Ph.D. candidate in Department of Materials Science & Engineering, Seoul National University, Seoul, Korea (Advisor: Prof. Heung Nam Han)

Mar. 2004 ~ Feb. 2008 : B.S. in Department of Materials Science & Engineering, Seoul National University, Seoul, Korea

Experience

Mar. 2008 ~ present : Researcher
Department of Materials Science & Engineering
College of Engineering, Seoul National University, Korea
< Main projects >

1. A simulation of FSW and analysis of thermo-mechanical properties in FSWed high strength steel
2. Development of analytical model and experimental method for prediction of properties of hot and cold coil
3. Development of prediction technology for microstructure and mechanical properties by a novel modeling method
4. Multi-scale mechanical property test and structural design technology for thin film solar cell
5. Development of properties analysis and optimized design technologies for high-functional 3D nano/micro structure system

Dec. 2012 ~June 2013 : Visiting researcher
School of Materials, The University of Manchester
Base: Research Complex at Harwell (RCaH), Rutherford Appleton Laboratory (RAL)
<Main Project>
A finite element model for function analysis of 4D-images based on laboratory and synchrotron (Advisor: Prof. Peter D. Lee)

Awards

1. Best paper award by 2011 Spring Conference of Korean Institute of Metals and Materials
2. Best paper award by 2011 5th Steel Science Forum
3. Best paper award by 2014 HumanTech Paper Award (Host: Samsung)

Papers

19. **Hoon-Hwe Cho**, Hae Lin Jang, Keunho Lee, Yigil Cho, Jimmy Xu, Ki Tae Nam and Heung Nam Han; Study of structural functionality of a ceramic biomaterial with pore size gradients using real structure based modeling, *in preparation*, 2014
18. **Hoon-Hwe Cho**, Sheng Yue, Yigil Cho, Heung Nam Han, and Peter D. Lee; Architectural responses of Ti foams with regular structure using micro-computed tomography and dual-level finite element modeling, *in preparation*, 2014
17. Dong-Wan Kim, **Hoon-Hwe Cho**, Won-Beom Lee, Kyun Taek Cho, Yi-Gil Cho, Se-Jong Kim and Heung Nam Han, Three-dimensional numerical investigation of phase transformation and deformation behavior during carburizing heat treatment for automotive gear ring, *in preparation*, 2014
16. Se-Jong Kim, Daeyong Kim, Keunho Lee, **Hoon-Hwe Cho** and Heung Nam Han; Enhanced formability of magnesium alloy sheet at room temperature due to texture evolution, *submitted*, 2014
15. **Hoon-Hwe Cho**, Yi-Gil Cho, Dong-Wan Kim, Hyun-Soo Cho, Won-Beom Lee and Heung Nam Han; Finite element investigation for edge wave prediction in hot rolled steel during run out table cooling, *ISIJ International*, Vol. 54, No. 7, pp. 1646-1652, 2014
14. Hyung-Seok Jang, Jung-Ho Lee, Yong-Sun Park, Young-O Kim, Jimin Park, Tae-Youl Yang, Kyoungsuk Jin, Jaehun Lee, Sunghak Park, Jae Myoung You, Ki-Woong Jeong, Areum Shin, In-Seon Oh, Min-Kyung Kwon, Yong-Il Kim, **Hoon-Hwe Cho**, Heung Nam Han, Yangmee Kim, Yoon Ho Chang, Seung R. Paik, Ki Tae Nam, Yoon-Sik Lee; Tyrosine-mediated two-dimensional peptide assembly and its role as a bio-inspired catalytic scaffold, *Nature Communications*, Vol. 5, No. 3665, doi:10.1038/ncomms4665, 2014
13. Md. Abu Mowazzem Hossain, Md. Tariqul Hasan, Sung-Tae Hong, Michael Miles, **Hoon-Hwe Cho** and Heung Nam Han; Mechanical behaviors of friction stir spot welded joints of dissimilar ferrous alloys under opening-dominant combined loads, *Advances in Materials Science and Engineering*, Vol. 2014, 572970, 2014
12. Md. Abu Mowazzem Hossain, Md. Tariqul Hasan, Sung-Tae Hong, Michael Miles, **Hoon-Hwe Cho** and Heung Nam Han; Failure behaviours of friction stir spot welded joints of dissimilar ferrous alloys under quasi-static shear loads, *International Journal of Materials and Product Technology*, Vol. 48, Nos. 1/2/3/4, pp. 179-193, 2014
11. Md. Abu Mowazzem Hossain, Md. Tariqul Hasan, Sung-Tae Hong, Michael Miles, **Hoon-Hwe Cho**, and Heung Nam Han; Friction stir spot welded joints of 409L stainless steels fabricated by a convex shoulder tool, *Metals and Materials International*, Vol. 19, No. 6, pp. 1243-1250, 2013
10. Yi-Gil Cho, Tae-Hong Ahn, **Hoon-Hwe Cho**, Jun Hyuk Moon, Shu Yang, Heung Nam Han, and Ju Li; Study of architectural responses of 3D periodic cellular materials, *Modelling and Simulation in Materials Science and Engineering*, Vol. 21, 065018, 2013
9. Jun-Yun Kang, Sang Hoon Lee, Yi-Gil Cho, Seul Cham Kim, **Hoon-Hwe Cho**, Heung Nam Han, Kyu Hwan Oh; Formation of Ultrafine Cellular Microstructure

Around Alumina Particles in a Low-Carbon Steel, *Metallurgical and Materials Transactions A*, Vol. 44, Issue 9, pp. 4098-4105, 2013

8. Moon-Jo Kim, **Hoon-Hwe Cho**, Sung-Hwan Kim, Seung Man Nam, Seung-Ha Lee, Man-been Moon and Heung Nam Han ; Effect of Zr addition on phase transformation and precipitation in B-added hot stamping steel, *Metals and Materials International*, Vol. 19, No. 4, pp. 629-635, 2013
7. **Hoon-Hwe Cho**, Sung-Tae Hong, Jae-Hun Roh, Hyun-Sik Choi, Suk Hoon Kang, Russell J. Steel, and Heung Nam Han; Three-dimensional numerical and experimental investigation on friction stir welding processes of ferritic stainless steel, *Acta Materialia*, Vol. 61, pp. 2649-2661, 2013
6. Chi-Sung Jeon, Sung-Tae Hong, Yong-Jai Kwon, **Hoon-Hwe Cho**, Heung Nam Han ; Material properties of friction stir spot welded joints of dissimilar aluminum alloys, *Transactions of Nonferrous Metals Society of China*, Vol. 22, pp. s605-s613, 2012
5. Yi-Gil Cho, Jin-You Kim, **Hoon-Hwe Cho**, Pil-Ryung Cha, Dong-Woo Suh, Jae Kon Lee, and Heung Nam Han; Analysis of Transformation Plasticity in Steel Using a Finite Element Method Coupled with a Phase Field Model, *PLoS ONE*, Vol. 7, e35987, 2012
4. **Hoon-Hwe Cho**, Suk Hoon Kang, Sung-Hwan Kim, Kyu Hwan Oh, Heung Ju Kim, Woong-Seong Chang, and Heung Nam Han; Microstructural Evolution in Friction Stir Welding of High-Strength Linepipe Steel, *Materials & Design*, Vol. 34, pp. 258-267, 2012
3. Dong-Wan Kim, Yi-Gil Cho, **Hoon-Hwe Cho**, Sung-Hwan Kim, Won-Beom Lee, Myoung-Gyu Lee, and Heung Nam Han; A Numerical Model for Vacuum Carburization of an Automotive Gear Ring, *Metals and Materials International*, Vol. 17, No. 6, pp. 885-890, 2011
2. **Hoon-Hwe Cho**, Heung Nam Han, Sung-Tae Hong, Jong-Hwan Park, Yong-Jai Kwon, Seok-Hyun Kim, and Russell J. Steel; Microstructural Analysis of Friction Stir Welded Ferritic Stainless Steel, *Materials Science and Engineering A*, Vol. 528, pp. 2889-2894, 2011

   ***** *Science Direct TOP25 Hottest Articles for January to March 2011*
1. **Hoon-Hwe Cho**, Yi-Gil Cho, Young-Roc Im, Jae Kon Lee, Jai-Hyun Kwak, and Heung Nam Han; A Finite Element Analysis for Asymmetric Contraction after Coiling of Hot-rolled Steel, *Journal of Materials Processing Technology*, Vol. 210, pp. 907-913, 2010